



**NAVAL
POSTGRADUATE
SCHOOL**

MONTEREY, CALIFORNIA

THESIS

**RELIABILITY AND RESILIENCE EVALUATION
OF A STAND-ALONE MOBILE MICROGRID-ANALYSIS
AND EXPERIMENTAL MEASUREMENTS**

by

David O. Jones

September 2022

Thesis Advisor:
Co-Advisors:

Giovanna Oriti
Preetha Thulasiraman
Douglas L. Van Bossuyt

Approved for public release. Distribution is unlimited.

THIS PAGE INTENTIONALLY LEFT BLANK

REPORT DOCUMENTATION PAGE			<i>Form Approved OMB No. 0704-0188</i>	
Public reporting burden for this collection of information is estimated to average 1 hour per response, including the time for reviewing instruction, searching existing data sources, gathering and maintaining the data needed, and completing and reviewing the collection of information. Send comments regarding this burden estimate or any other aspect of this collection of information, including suggestions for reducing this burden, to Washington headquarters Services, Directorate for Information Operations and Reports, 1215 Jefferson Davis Highway, Suite 1204, Arlington, VA 22202-4302, and to the Office of Management and Budget, Paperwork Reduction Project (0704-0188) Washington, DC 20503.				
1. AGENCY USE ONLY (Leave blank)		2. REPORT DATE September 2022	3. REPORT TYPE AND DATES COVERED Master's thesis	
4. TITLE AND SUBTITLE RELIABILITY AND RESILIENCE EVALUATION OF A STAND-ALONE MOBILE MICROGRID-ANALYSIS AND EXPERIMENTAL MEASUREMENTS			5. FUNDING NUMBERS	
6. AUTHOR(S) David O. Jones				
7. PERFORMING ORGANIZATION NAME(S) AND ADDRESS(ES) Naval Postgraduate School Monterey, CA 93943-5000			8. PERFORMING ORGANIZATION REPORT NUMBER	
9. SPONSORING / MONITORING AGENCY NAME(S) AND ADDRESS(ES) N/A			10. SPONSORING / MONITORING AGENCY REPORT NUMBER	
11. SUPPLEMENTARY NOTES The views expressed in this thesis are those of the author and do not reflect the official policy or position of the Department of Defense or the U.S. Government.				
12a. DISTRIBUTION / AVAILABILITY STATEMENT Approved for public release. Distribution is unlimited.			12b. DISTRIBUTION CODE A	
13. ABSTRACT (maximum 200 words) <p>As the Department of Defense (DOD) deploys renewable distributed energy resources (DERs) to reduce fossil fuel consumption, microgrids are being evaluated as one way to generate and deliver reliable electric power to stationary and mobile military units. Commercial off the Shelf (COTS) microgrid components are a viable cost-effective option to setup stand-alone microgrid systems to support mobile military units and help drive the transition to a more sustainable yet energy-resilient military. Reliability and resilience are key parameters in determining the effectiveness of microgrids in supporting military missions. Although in the past few years many researchers have presented reliability and resilience models of various complexity, experimental measurements and model validation are not available in the literature for mobile COTS microgrids. The goal of this thesis research is to experimentally assess the reliability and resilience of stand-alone, mobile microgrids that can be carried by one or two individuals and can be easily assembled in the field in support of operations in locations where utility power is not available. Utilizing COTS DERs including batteries, PV arrays and power converters, three different standalone microgrid architectures were designed, analyzed, and tested in the laboratory. Reliability block diagrams, and system fault trees were created per MIL-HDBK-338B, to compare the reliability of the three microgrid configurations.</p>				
14. SUBJECT TERMS microgrid, stand-alone microgrid, off-grid, solar, photovoltaic, PV, batteries, distributed energy resources, DERs, Commercial off the Shelf, COTS			15. NUMBER OF PAGES 111	
			16. PRICE CODE	
17. SECURITY CLASSIFICATION OF REPORT Unclassified	18. SECURITY CLASSIFICATION OF THIS PAGE Unclassified	19. SECURITY CLASSIFICATION OF ABSTRACT Unclassified	20. LIMITATION OF ABSTRACT UU	

THIS PAGE INTENTIONALLY LEFT BLANK

Approved for public release. Distribution is unlimited.

**RELIABILITY AND RESILIENCE EVALUATION OF A STAND-ALONE
MOBILE MICROGRID-ANALYSIS AND EXPERIMENTAL MEASUREMENTS**

David O. Jones
Major, United States Marine Corps
BS, United States Naval Academy, 2010

Submitted in partial fulfillment of the
requirements for the degree of

MASTER OF SCIENCE IN ELECTRICAL ENGINEERING

from the

**NAVAL POSTGRADUATE SCHOOL
September 2022**

Approved by: Giovanna Oriti
Advisor

Preetha Thulasiraman
Co-Advisor

Douglas L. Van Bossuyt
Co-Advisor

Douglas J. Fouts
Chair, Department of Electrical and Computer Engineering

THIS PAGE INTENTIONALLY LEFT BLANK

ABSTRACT

As the Department of Defense (DOD) deploys renewable distributed energy resources (DERs) to reduce fossil fuel consumption, microgrids are being evaluated as one way to generate and deliver reliable electric power to stationary and mobile military units. Commercial off the Shelf (COTS) microgrid components are a viable cost-effective option to setup stand-alone microgrid systems to support mobile military units and help drive the transition to a more sustainable yet energy-resilient military. Reliability and resilience are key parameters in determining the effectiveness of microgrids in supporting military missions. Although in the past few years many researchers have presented reliability and resilience models of various complexity, experimental measurements and model validation are not available in the literature for mobile COTS microgrids. The goal of this thesis research is to experimentally assess the reliability and resilience of stand-alone, mobile microgrids that can be carried by one or two individuals and can be easily assembled in the field in support of operations in locations where utility power is not available. Utilizing COTS DERs including batteries, PV arrays and power converters, three different standalone microgrid architectures were designed, analyzed, and tested in the laboratory. Reliability block diagrams, and system fault trees were created per MIL-HDBK-338B, to compare the reliability of the three microgrid configurations.

THIS PAGE INTENTIONALLY LEFT BLANK

Table of Contents

1 INTRODUCTION	1
1.1 Related Work	1
1.2 Research Objectives and Contribution	2
1.3 Organization	3
2 BACKGROUND	5
2.1 Distributed Energy Resources and Stand-Alone Microgrids.	5
2.2 Reliability Analysis of Electronic Systems	6
2.3 Reliability and Failure Models	10
2.4 Sizing Microgrid Components to Improve System Reliability	14
3 MICROGRID CONFIGURATIONS AND RELIABILITY MODELING	29
3.1 Microgrid Architectures with Varying Numbers of DERs	29
3.2 Increasing Reliability with Spare Parts	45
3.3 Reliability Estimate and Comparison of the Three Configurations	46
4 EXPERIMENTAL MEASUREMENTS AND RESULTS	49
4.1 Experimental Microgrid Set-up.	49
4.2 Experimental Measurements	60
4.3 Microgrid Resilience Analysis	80
4.4 Availability	82
5 CONCLUSION AND FUTURE WORK	83
5.1 Future Work	84
List of References	85
Initial Distribution List	91

THIS PAGE INTENTIONALLY LEFT BLANK

List of Figures

Figure 2.1	Hazard rate as a function of age	7
Figure 2.2	A series network	11
Figure 2.3	A parallel network with two components	11
Figure 2.4	A parallel network with three components	12
Figure 2.5	Sample fault tree analysis format and symbology	13
Figure 2.6	Inputs and outputs of manual design tool	16
Figure 2.7	Inputs and outputs of automatic tool	17
Figure 2.8	Comparison of energy densities and specific energy of different rechargeable batteries	19
Figure 2.9	Days of battery storage needed for a stand-alone system with 95% and 99% system availability. Peak sun hours are on a month-by-month basis. Based on Sandia Laboratories	20
Figure 2.10	Lead-acid battery capacity depends on discharge rate and temperature	24
Figure 2.11	PV I-V curve	26
Figure 2.12	Hourly irradiation curve	27
Figure 2.13	I-V curve of photovoltaics with no maximum power point tracking	28
Figure 3.1	Architecture of configuration 1	30
Figure 3.2	Parallel photovoltaic arrays, at any given voltage the currents add	31
Figure 3.3	Architecture of configuration 2	32
Figure 3.4	Modules in series, at any given current the voltages add	33
Figure 3.5	Architecture of configuration 3	34
Figure 3.6	Reliability block diagram for microgrid configuration 1	35

Figure 3.7	System fault tree for microgrid configuration 1	37
Figure 3.8	Microgrid configuration 1 reliability diagram with spares readily available	38
Figure 3.9	Reliability block diagram for microgrid configuration 2	39
Figure 3.10	System fault tree for microgrid configuration 2	40
Figure 3.11	Microgrid configuration 2 reliability diagram with spares readily available	41
Figure 3.12	Reliability block diagram for microgrid configuration 3	42
Figure 3.13	System fault tree for microgrid configuration 3	44
Figure 3.14	Microgrid configuration 3 reliability diagram with spares readily available	45
Figure 4.1	Notional block diagram of the experimental setup	49
Figure 4.2	Solartech photovoltaic array	51
Figure 4.3	Tracer4210AN maximum power point tracking solar charge controller	52
Figure 4.4	12 V 100AH deep cycle absorbent glass mat battery	53
Figure 4.5	Circuit breaker magnetic-hydraulic lever	54
Figure 4.6	DC to AC power inverters	55
Figure 4.7	AC critical load display	57
Figure 4.8	Fluke 434 power quality analyzer	58
Figure 4.9	MT50 remote meters and maximum power point tracking solar charge controllers	60
Figure 4.10	Bidirectional volt/amp meter	60
Figure 4.11	Solar radiation data in Monterey, CA	61
Figure 4.12	Photovoltaic power potential in the United States of America	61

Figure 4.13	Experimental voltage plot for test 10 (AC power increment 200 W)	66
Figure 4.14	Experimental current plot for test 10 (AC power increment 200 W)	67
Figure 4.15	Experimental power plot for test 10 (AC power increment 200 W)	68
Figure 4.16	Experimental voltage plot for the stress test	69
Figure 4.17	Experimental current plot for the stress test	70
Figure 4.18	Experimental power plot for the stress test	71
Figure 4.19	Experimental voltage plot for test 20	74
Figure 4.20	Experimental current plot for test 20	75
Figure 4.21	Experimental power plot for test 20	76
Figure 4.22	Experimental voltage plot for test 26	78
Figure 4.23	Experimental current plot for test 26	79
Figure 4.24	Experimental power plot for test 26	80

THIS PAGE INTENTIONALLY LEFT BLANK

List of Tables

Table 2.1	Minimum system voltages based on limiting current to 100 A . . .	21
Table 2.2	Models of batteries	22
Table 2.3	Example deep-cycle lead-acid battery characteristics	23
Table 2.4	Temperature correction factor of lead-acid and Li-ion batteries . . .	25
Table 3.1	Theoretical probability of success with spares available for each configuration	48
Table 4.1	Specification of the photovoltaic arrays used in the experiment . . .	50
Table 4.2	Specification of the Tracer4210 maximum power point tracking solar charge controller used in the experiment	52
Table 4.3	Specification of the 12 V 100 AH deep cycle absorbent glass mat battery	53
Table 4.4	Specification of the circuit breaker magnetic-hydraulic lever	54
Table 4.5	Specification of the DC-AC power inverter	55
Table 4.6	AC critical load description	56
Table 4.7	Fluke 434 settings	59
Table 4.8	Experimental data for configuration 1	64
Table 4.9	Experimental data for configuration 2	73
Table 4.10	Experimental data for configuration 3	77
Table 4.11	Total data for each configuration	81

THIS PAGE INTENTIONALLY LEFT BLANK

List of Acronyms and Abbreviations

AC	Alternating Current
AGM	Absorbent Glass Mat
BATT	Battery
COTS	Commercial off the Shelf
DC	Direct Current
DERs	Distributed Energy Resources
DOD	Department of Defense
ESS	Energy Storage Systems
FTA	Fault Tree Analysis
LCD	Liquid Crystal Display
LED	Light-Emitting Diode
MASINT	Measurement and Signature Intelligence
MDOD	Maximum Depth of Discharge
MPP	Max Power Point
MPPT	Maximum Power Point Tracker
MS	Microsoft
MTBF	Mean Time Between Failure
MTTF	Mean Time To Failure
MTTR	Mean Time To Repair

NPS	Naval Postgraduate School
PC	Personal Computer
PSH	Peak Sun Hours
PV	Photovoltaic
RBD	Reliability Block Diagram
RESS	Renewable Energy Storage Systems
RMS	Root Mean Square
SCC	Solar Charge Controller
SPST	Single Pole Single Throw
SRWBR	Short Range Wide Band Radio
TCF	Temperature Correction Factor
TCP	Transmission Control Protocol
USMC	U.S. Marine Corps
USN	U.S. Navy

Acknowledgments

I would like to earnestly acknowledge the sincere efforts and valuable time given by my thesis advisor, Dr. Giovanna Oriti, as well as Dr. Douglas Van Bossuyt for their support of my thesis research efforts.

I would also like to acknowledge lab technicians Mr. Jeff Knight and Mr. Franklin Blevins for their unwavering support, guidance, and countless safety inspections of the stand-alone microgrid. They never hesitated to support my research efforts and were always available for questions.

Lastly, I would like to thank my family for their constant love and support. Without that support, this would not be possible. Thank you!

THIS PAGE INTENTIONALLY LEFT BLANK

CHAPTER 1: INTRODUCTION

As outlined in Executive Order 14057, the Federal Government is directed to lead the nation in an effort to significantly reduce carbon emissions on Department of Defense (DOD) installations by 2035 in order to reach net-zero emissions economy-wide no later than 2050 [1]. The U.S. Navy (USN) and U.S. Marine Corps (USMC) are contributing to this goal by deploying more and more renewable Distributed Energy Resources (DERs) in facilities and forward operating bases to reduce fossil fuel consumption. DERs are often controlled together in a system known as a microgrid, which has been extensively studied and discussed in recent years [2]–[10]. Design tools and models are needed to properly size DERs and to setup microgrids that can generate and distribute reliable power to support stationary and mobile military units. This research aims to examine the reliability and resilience of a stand-alone microgrid with the possibility of built-in redundancy. Theoretical reliability will be analyzed based on the Commercial off the Shelf (COTS) components and resilience will be analyzed through a multitude of laboratory experiments designed to stress the system and examine its ability to withstand and minimize impact to the overall performance. In an enemy-contested environment, users will need a reliable yet resilient power system that is capable of responding to disruptions and continue providing power to meet mission success.

1.1 Related Work

In recent years, a few research studies focusing on the design and resilience of stand-alone microgrids for military applications have been published [2]–[5], [7], [11]–[13]. In [7] the authors review the “vital aspects of DER based microgrids and present simulations to investigate the impacts of DER sources, electric vehicles (EV) and Energy Storage Systems (ESS) on practicable architectures’ resilient operation.” In [4] a system engineering approach was used to evaluate microgrid resilience while accounting for its impact on a military mission. Novel resilience definitions and analyses were applied to standalone microgrids in [5].

As described in [2], [12] a design method was created for user to accurately size DERs of a microgrid systems to meet load requirements when utility power is not available. In [13] the design tool was expanded to hybrid microgrids that operate in different geographical locations and environments, that includes variations of both temperature and solar insolation. A simulation-based modeling framework for rightsizing hybrid microgrids is proposed in [3] for systems composed of diesel generators, a Photovoltaic (PV) system, a battery ESS and an energy management system.

Lastly [14] presents a “framework of reliability assessment and varying characteristics of analysis aiming at PV-ESS based stand-alone MG has been developed, by taking the sequential stochastic states of the main components of MG, minimization of a load shedding model, as well as CL model into consideration.”

From the above literature review, the following gap was identified; although microgrid resilience has been defined and analyzed with extensive simulation work such as [4], [5], not much experimental work has been presented in support of the analysis. This research aims to explore the reliability and resilience of a stand-alone microgrid on a laboratory testbed using COTS products, in addition to military handbooks 217F and 338B [15], [16].

1.2 Research Objectives and Contribution

As the literature has shown, resilience and reliability are key factors in determining the appropriate number of DERs that is most effective to support a military mission. Although much literature exists on these topics, experimental data is not available to evaluate the resilience and reliability of COTS microgrids. The primary objective of this thesis is to evaluate the resilience and reliability of a COTS stand-alone microgrid using statistical analysis and experimental measurements.

To accomplish the primary objective, first sizing and design of the stand-alone microgrid was conducted. Using available COTS DERs and components, three different configurations were designed based on the manufacturer specifications outlined in each manual. The theoretical reliability models and system fault trees were then created and analyzed to estimate and compare the reliability of the three microgrid configurations and to explore potential causes of system level failure using the methods outlined in Military Handbooks

338B and 217F [15], [16]. Additionally, statistical distribution functions were used to predict how redundancy and spare parts affect microgrid reliability. After the reliability analysis, an extensive experimental study evaluated the resilience of the three microgrid configurations on a laboratory testbed.

1.3 Organization

The remainder of this thesis is organized as follows: Chapter 2 covers some background information to include DERs as part of stand-alone microgrid systems, reliability analysis of electronic components, and sizing of those components based on reliability.

Chapter 3 covers the design of three microgrid configurations using COTS components. It also presents the reliability and resilience analysis of the COTS microgrids using the Reliability Block Diagram (RBD) and Fault Tree Analysis (FTA) methods to compare the three configurations and evaluate the effects of redundancy and spare parts on improving system reliability. Potential ways of system level failures are also discussed.

Chapter 4 contains a detailed description of the microgrid testbed and its components, the results from the experiments, and a discussion of the resilience of the microgrid configurations including the impact of redundancy.

Chapter 5 summarizes the results obtained from the design, analysis and experiments, and it also presents potential future work pertaining to stand-alone microgrids for mobile military operations.

THIS PAGE INTENTIONALLY LEFT BLANK

CHAPTER 2: BACKGROUND

Microgrids and the use of DERs are changing the way energy is produced, stored, and distributed. This chapter will review stand-alone microgrids and the use of DERs. Additionally, reliability analysis of electronic systems will be reviewed using methods outlined in military handbooks 217F and 338B [15], [16]. The proper sizing of microgrid components based on reliability will also be discussed.

2.1 Distributed Energy Resources and Stand-Alone Microgrids

Electrical energy is arguably one of the most universally used elements in the world [7]. The use of conventional energy resources to produce electrical energy is a topic of discussion because fuel energy resources are proven to be the cause of the rapid increase in global carbon emission levels [1], [17]. Sustainable means to produce electrical energy are now at the forefront of research and development in an effort to significantly reduce carbon emissions. In recent years renewable energy sources such as wind, solar, tidal, bioenergy, etc. have become very attractive for the global production of sustainable energy and the quest towards a greener future [18]. Renewables such as wind and solar are considered environmentally friendly DERs which can contribute to the setup of resilient microgrid systems.

In [9] the author states, “DERs encompass a wide range of power generation technologies, such as internal combustion engines, gas turbines, microturbines, PV systems, fuel cells, and wind power.” This technology is commonly associated with renewable energy resources and microgrid systems. Pairing DERs with microgrid systems physically reduces the electrical distance between the power generation and electrical loads [9]. When sources are closer to electrical loads that yields a reduction in losses, a reduction in transmission bottlenecks, and a greater use of wasted heat [9].

Microgrid research, development, and implementation has been accelerated in recent years as a method to increase the use of renewable energy resources to generate electrical power [19]. Microgrids are active distribution systems that include DERs, such as distributed generation and distributed storage, and can operate in either grid-connected or islanded mode (stand-alone) [8] and IEEE standard 1547-2018 can also be used to identify how DERs should be connected. As identified in [8], “The main goals of microgrids are to improve distribution reliability, support high penetration of renewable energy, to offer islanding capability, and to improve generation efficiency in a sustainable power grid.” Stand-alone microgrids using more economic and environmentally sustainable DERs provide a certain level of independence from the utility grid. Stand-alone systems do not have to worry about how the systems affects anyone else and can be configured to support the specific needs of the user, independent of grid-tied regulations. Additionally, stand-alone microgrids completely isolate users from grid power outages or security breaches [10].

2.2 Reliability Analysis of Electronic Systems

Power electronic systems are the enabling technology for DERs as utility interfaces to renewable energy resources and energy storage systems [20]. Researchers have placed much emphasis on reliability and resilience of power electronic systems. In recent years, much emphasis has been placed on the reliability and resilience of power electronic systems [21], [22]. References [15], [23], [24] uses mathematical estimations to show various methods of analyzing the reliability of electronic systems. An analysis of component level failure models were examined extensively in [20], [25]–[27]. In [20] several analytical methodologies are presented to build system level reliability models with the goal of producing accurate reliability predictions. Various solutions are proposed to improve reliability. Spare parts availability, inherent redundancy, active online monitoring, and management of faults are among several methods to enhance reliability [20], [28]–[30].

In analyzing ways to improve overall system level reliability the metric needs to be analyzed. Metrics ultimately reflect the design goal which is driven by user requirements. The commonly adopted metrics to evaluate the reliability of electronic systems are failure rate, Mean Time To Failure (MTTF), Mean Time Between Failure (MTBF), Mean Time To Repair (MTTR), and availability [20].

Failure rate as defined in [16] is “the total number of failures within an item population, divided by the total number of life units expended by that population, during a particular measurement period under stated conditions.” In other words, it is an indication of susceptibility to failure after a specific time period for a component or system. Figure 2.1 shows a typical failure rate curve as a function of time, referred to as the “bathtub curve” [16]. The plot in Figure 2.1 suggests that life cycles can be divided into periods: the “infant mortality period,” “useful life period,” and the “wear-out period” [16]. Items are subjected to extensive testing prior to fielding, which result in removal of the infant mortality period prior to use. Undiscovered defects in design and production greatly contributes to high failure rate in the infant mortality period [20]. When an item survives the infant mortality period, the failure rate stabilizes over a constant time period prior to reaching the wear-out period. During the wear-out period, systems generally have completed their required mission and failure rates increase [20]. At this point it is vital to conduct a reliability analysis to determine the probability of success for continued use of the item.

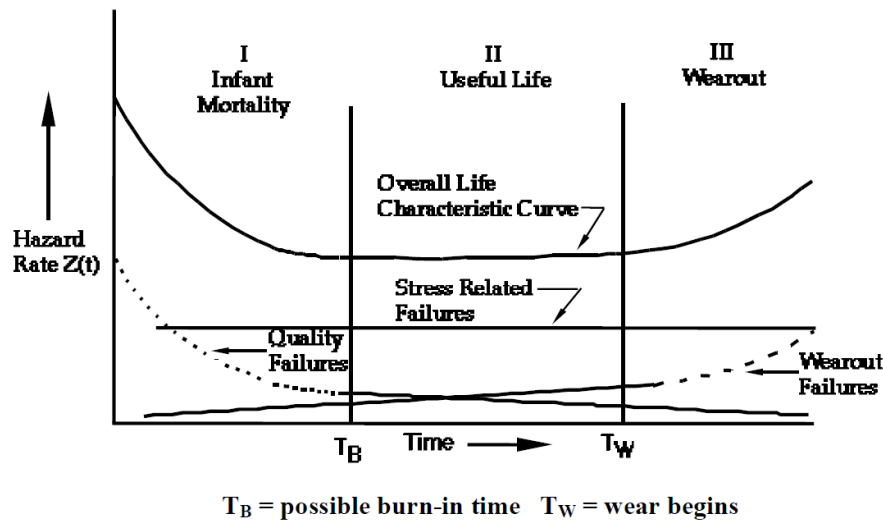


Figure 2.1. Hazard rate as a function of age. Source [16].

The reliability function, $R(t)$, or the probability that an item has not failed prior to time t , as described in [16], is expressed as,

$$R(t) = 1 - F(t) = \int_t^{\infty} f(t)dt. \quad (2.1)$$

It goes on to say that the “failure rate $\lambda(t)$, is defined as the ratio of probability that failure occurs in the interval, given that it has not occurred prior to time t , the start of the interval, divided by the interval length” [16]. In [16], the equation is expressed as

$$\lambda(t) = \frac{R(t) - R(t + \Delta t)}{\Delta t R(t)}. \quad (2.2)$$

Additionally, “the hazard rate, $h(t)$, or instantaneous failure rate, is defined as the limit of the failure rate as the interval length approaches zero” [16]. In [16], the equation is expressed as

$$h(t) = \lim_{\Delta t \rightarrow 0} \frac{R(t) - R(t + \Delta t)}{\Delta t R(t)}. \quad (2.3)$$

Furthermore, “the reliability function $R(t)$ is determined from the failure rate $h(t)$ with the assumption of $R(0) = 1$, i.e. the item is fully functional at the initial state” [16]. In [16], the equation is expressed as

$$R(t) = e^{-\int_0^t h(t)dt}. \quad (2.4)$$

“In many reliability models, the failure rates of components and subsystems are assumed independent of time although this assumption has limitations” [16]. In [16], [20], [30], the equation is expressed as

$$R(t) = e^{-\lambda t}. \quad (2.5)$$

In many cases for electronics equipment, equation (2.4) becomes equation (2.5) for the exponential distribution function.

Time, an important aspect of reliability analysis, can be expressed in terms of MTTF or MTBF [30]. MTTF is the expected time prior to failure occurring. MTTF does not depend on a specific time period, which is different from reliability. It gives the mean time of an item operating without failing as described in [16], [20]. In [16], the equation is expressed as

$$MTTF = \int_0^{\infty} R(t)dt. \quad (2.6)$$

MTBF appears very often in reliability literature. “It applies to the repairable items in which failed elements are replaced upon failure” [16]. In [16], [20], [30], MTBF is expressed as

$$MTBF = \frac{1}{\lambda}. \quad (2.7)$$

Military Handbook 338 [16] describes availability as “the probability that a system is operating satisfactorily at any random point in time t , when subject to a sequence of ‘up’ and ‘down’ cycles which constitute an alternating renewal process” [16]. Operational availability is the “probability that a system or equipment, when used under stated conditions in an actual operational environment, will operate satisfactorily when called upon” [30]. In [16], operational availability is expressed as

$$A_o = \frac{MTBM + RT}{MTBM + RT + MDT} \quad (2.8)$$

where,

$$MTBM = \frac{1}{(\lambda + f)} \quad (2.9)$$

and,

$$MDT = \bar{M} + \text{Mean Logistic Time} + \text{Mean Administrative Time}. \quad (2.10)$$

The \bar{M} as described in [16] is “the mean active and corrective preventative maintenance time and MTBM is the mean interval between corrective and preventive maintenance actions equal to the reciprocal of the frequency at which these actions occur, which is the sum of the frequency or rate (λ) at which corrective maintenance actions occur and the frequency or rate (f) at which preventive maintenance actions occur.” RT is the system average ready time, meaning the system is ready but not actually available in an operational cycle [16].

2.3 Reliability and Failure Models

Reliability modeling provides a process for predicting or understanding the reliability of each component within a system. Military Handbook 338B states that reliability models are used for prediction and for estimation [16].

2.3.1 Reliability Block Diagrams

The common diagrammatic methods used to predict the reliability of success and failure of a system is through the use of RBDs. “RBDs are constructed to show interdependencies among all elements (subsystems, equipment, etc.) or functional groups of the item for item success in each service use event” [16]. RBDs are a visual depiction of the system success through the use of various series-parallel paths [16].

In reference [30] the author states, “the series relationship is probably the most common used and is the simplest to analyze.” This analysis is illustrated in Figure 2.2, each subcomponent must be functional if the system is to operate properly [30]. The expressions is represented by the product of the reliabilities of the individual subcomponents as described in [16], [30], as

$$R = (R_A)(R_B)(R_C). \quad (2.11)$$

If a series system is expected to operate for a specific time period, it can be expressed as described in [30], as

$$R_S = (e^{-\lambda_1 t})(e^{-\lambda_2 t})(e^{-\lambda_3 t}) \dots (e^{-\lambda_n t}). \quad (2.12)$$

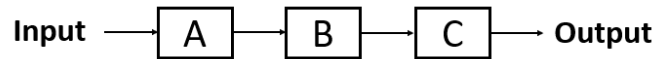


Figure 2.2. A series network

“A pure parallel network is one where several of the same components are in parallel and where all the components must fail to cause total system failure” [30]. The reliability for a two-component system assuming the components are identical and the system will function if A or B, or both, are working, as defined in [30], is

$$R = R_A + R_B - (R_A)(R_B). \quad (2.13)$$

Figure 2.3 illustrates the parallel two component system.

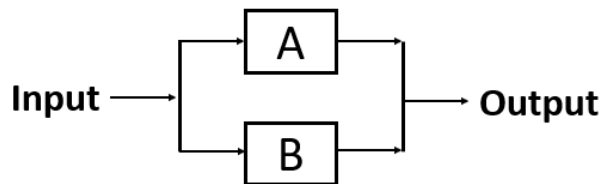


Figure 2.3. A parallel network with two components

A network with three components in parallel as shown in Figure 2.4 as defined in [30], is

$$R = 1 - (1 - R_A)(1 - R_B)(1 - R_C). \quad (2.14)$$

If all components A-C are identical, the reliability expression as define in [30] and illustrated in Figure 2.4, is

$$R = 1 - (1 - R)^3. \quad (2.15)$$

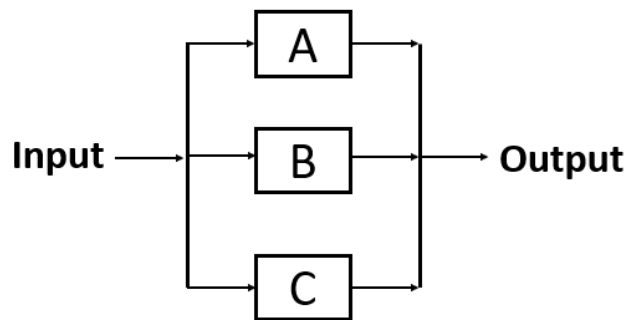
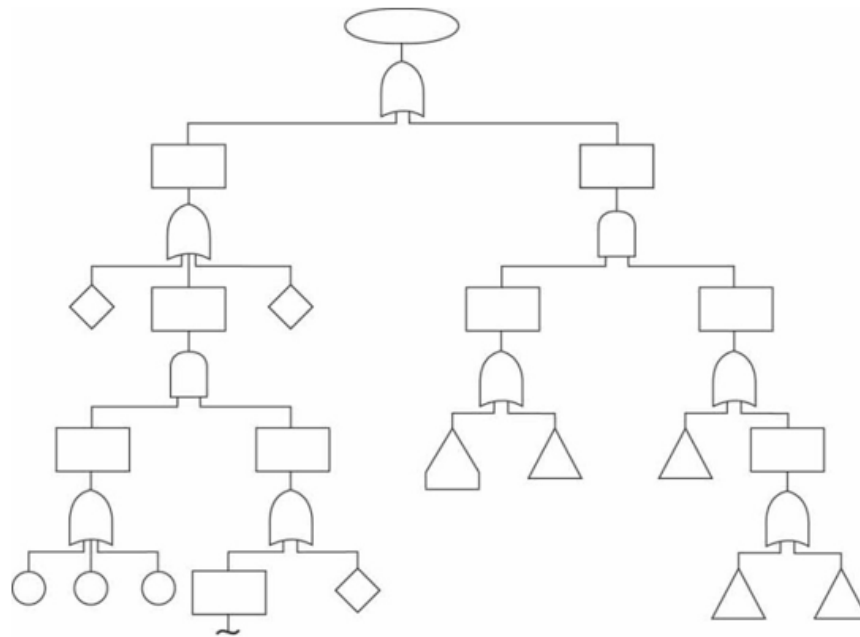
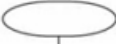


Figure 2.4. A parallel network with three components

2.3.2 Fault Tree Analysis

The FTA is a deductive approach and analysis of multiple ways that failure could occur and the probability of occurrence [30]. “It is a top-down fault tree structure that is developed for each critical failure mode. A fault tree helps users understand how the system can fail and helps in identifying best ways to reduce risk or to determine event rates of a safety accident or a particular system level failure” [30]. Figure 2.5 illustrates a sample fault tree analysis and symbology.



- 

The ellipse represents the *top-level event*. Obviously, the ellipse always appears at the very top of a fault tree.
- 

The rectangle represents an *intermediate fault event*. A rectangle can appear anywhere in a tree except at the lowest level in the hierarchy.
- 

A circle represents the *lowest-level failure event*, also called a *basic event*. Basic events are likely to appear at the lowest level in a fault tree.
- 

The diamond represents an *undeveloped event*. Undeveloped events could be further broken down, but are not for the sake of simplicity. Very often, complex undeveloped events are analyzed through a separate fault tree. Undeveloped events appear at the lowest level in a fault tree.
- 

This symbol, sometimes called the house, represents an *input event*. An input event refers to a signal or input that could cause a system failure.
- 

This symbol represents the *AND logic gate*. In this case, the output is realized only after all the associated inputs have been received.
- 

This symbol represents the *OR logic gate*. In this case, any one or more of the inputs need to be received for the output to be realized.

Figure 2.5. Sample fault tree analysis format and symbology. Source [30].

2.3.3 Exponential Distribution

The exponential distribution is an important distribution that is commonly used in reliability analyses for prediction of electronic equipment failures [15], [16]. The exponential function describes the situation wherein the hazard rate $h(t)$ is constant and is generated by the Poisson process [16].

The failure density function described in [16] is,

$$f(t) = \lambda e^{-\lambda t} \quad \text{for } t > 0, \quad (2.16)$$

where λ is the hazard (failure) rate, and the reliability function is,

$$R(t) = e^{-\lambda t}. \quad (2.17)$$

Some applications of the exponential model include but are not limited to: “items whose failure rate does not change significantly with age; complex and repairable equipment without excessive amounts of redundancy; and equipment for which the early failures or ‘infant mortalities’ have been eliminated by ‘burning in’ the equipment for some reasonable time period” [16]. The exponential function is applicable for conducting an analysis of individual components that makes up the overall system.

2.4 Sizing Microgrid Components to Improve System Reliability

Selecting the size of DERs in the planning phase is vital when designing a microgrid system [3]. Several articles have been published on the evaluation criteria for the correct sizing of stand-alone PV systems [2], [31], [32] and IEEE standard 1562-2007. An adequately designed and sized stand-alone microgrid system will operate independently from the commercial grid and supply enough power to support the critical load for the duration of the mission [3], [11], [12]. This includes the number, type and rating of PV arrays, the

capacity and number of batteries, inverter rating, Maximum Power Point Tracker (MPPT) charge controllers and cables [33]. This section is designed to inform planners on a method to properly sizing a stand-alone microgrid using batteries as ESS, and PVs as the power source.

The design tool discussed in this section comprises two sections: the battery bank system as the ESS, and the PV arrays [12]. The Microsoft (MS) excel document developed by prior thesis student [13] was used for the stand-alone microgrid configurations. Figures 2.6 and 2.7 shows two different automation tools, the manual and automatic, with numbers based on the design for a 6.2 kWh/day stand-alone microgrid located in Monterey, California. The generator and fuel fields are not used since there is no generator in this microgrid design.

Inputs		Outputs		
Battery Bank Design		Battery Bank Design		
User Inputs		Outputs		
System and Load Specifications		Batteries in series	2	
1	Inverter efficiency	0.9	Batteries in parallel	2
2	AC Load total (kWh/day)	0.264	Total number of batteries	4
3	AC Load Critical (kWh/day)	0.222	Minimum state of charge in NOC (%)	72
4	System Voltage	24		
Battery Specifications		PV Design		
5	Battery Voltage (volts)	12	Number of Modules in series	1
6	Capacity (Ah/battery)	100	Number of Modules in parallel	2
7	Efficiency (as a decimal)	0.94	Modules Total	2
8	MDOD (as a decimal)	0.8	PV output (Ah)	27.2986
9	Battery Type & Temperature Range (°C)	LA Temp ≥ 25	PV output (kWh/day)	0.655
User Preferences		Generator Design		
#	Required Usable Storage for Total Load (days)	1	Number of generators	0
#	Required Usable Storage for Critical Load (days)	3	Maximum number of generators based on min charge time	0
PV Design		Fuel Storage Design		
User Inputs		Outputs		
Environmental Factors		Storage capacity needed (gal)	0	
#	Peak Sun Hours (kWh/m ²)	6.2	Number of fuel containers needed	0
PV Specifications				
#	MPP Current (amps)	2.59		
#	MPP Voltage (volts)	35		
User Preferences				
#	Solar fraction	1		
#	MPPT?	Yes		
#	Array to Load ratio	1.2		
Generator and Fuel Storage Design		User Inputs		
#	Maximum load power (kW)	0		
#	Generator rated power (kW)	0		
#	Fuel storage container capacity (gal)	0		
#	Generator Fuel rate (gal/hr)	0		
#	Required Days of Autonomy	0		

Figure 2.6. Inputs and outputs of manual design tool. Adapted from [13].

Inputs		Outputs	
Battery Bank Design	User Inputs	Battery Bank Design	Outputs
System and Load Specifications		Batteries in series	2
Inverter efficiency	0.9	Batteries in parallel	2
AC Load total (kWh/day)	0.264	Total number of batteries	4
AC Load critical (kWh/day)	0.222	Minimum state of charge in NOC (%)	72
System Voltage (v)	24		
Battery Specifications		PV Design	Outputs
Battery Model	Relion RB48V200	Number of Modules in series	0
Battery Type & Temperature Range (°C)	LA Temp≥25	Number of Modules in parallel	3
User Preferences		Modules Total	1
Required Usable Storage for Total Load (days)	1	PV output (Ah)	96.2829
Required Usable Storage for Critical Load (days)	3	PV output (kWh/day)	2.31079
PV Design		Generator Design	Outputs
Environmental Factors		Number of generators	0
Peak sun hours (kWh/m ²)	6.2	Maximum number of generators based on min charge time	0
PV Specifications			
PV Model	SunPower SPR-X22-36		
User Preferences		Fuel Storage Design	Outputs
Solar fraction	1	Storage capacity needed (gal)	0
Array to Load ratio	1.2	Number of SIXCONs needed	0
MPPT?	Yes	Number of other containers needed	0
Generator and Fuel Storage Design			
User Inputs			
Maximum load power (kW)	0		
Generator Model and Rated Power	30kW AMMPS		
Fuel storage container type	SIXCON		
Other Fuel storage capacity (gallons)	0		
Required Days of Autonomy	0		

Figure 2.7. Inputs and outputs of automatic tool. Adapted from [13].

2.4.1 Battery Description and Sizing

The most commonly used ESS found in stand-alone microgrids include rechargeable batteries. Figure 2.8 compares the energy densities of the various commercial rechargeable batteries currently in use. Lead-acid batteries that are designed and built for deep cycle applications are produced in three different categories: flooded, gel sealed, and Absorbent Glass Mat (AGM) sealed [34]. Lead-acid batteries are widely used in the USN. “Li-ion batteries are highly advanced as compared to other commercial rechargeable batteries, in terms of geometric and volumetric energy” [35]. Figure 2.8 clearly show the superiority of Li-ion batteries, which is the most popular and widely used battery source in electronic devices today. Li-ion batteries were established for use as an ESS due to their small size, lighter weight, longer lifetime, and higher capacity [12]. However, they are still considered a fire-hazard by the USN and they are not used in naval facilities as widely as they are used commercially.

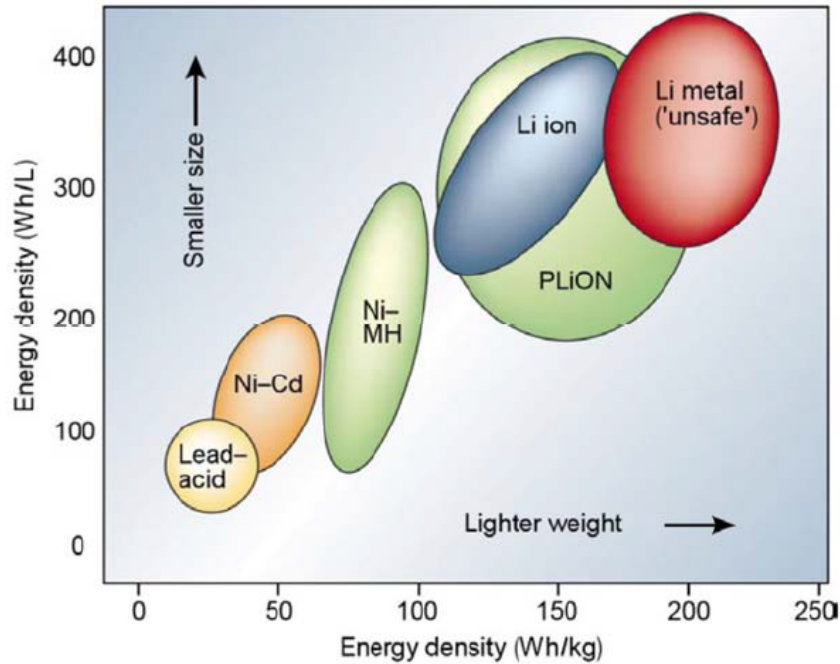


Figure 2.8. Comparison of energy densities and specific energy of different rechargeable batteries. Source [35].

Prior to determining the size of the batteries needed to sustain operation for the stand-alone microgrid, it is appropriate to calculate the battery capacity [12].

The load power design presented in this design tool is in kWh and the Alternating Current (AC) load is in kWh/day as shown in Figures 2.6 and 2.7. The autonomy period is another key aspect in the battery design. It is the time period in which the load is completely powered by a fully charged battery bank system [36]. This essentially means the battery bank will not receive power from the PV arrays. Sizing a ESS to meet demand, “99% of the time can easily cost triple that of one that meets demand only 95% of the time” [36]. Figure 2.9 can be utilized to estimate the number of days of storage that can be provided by the system as described in the guidebook [37].

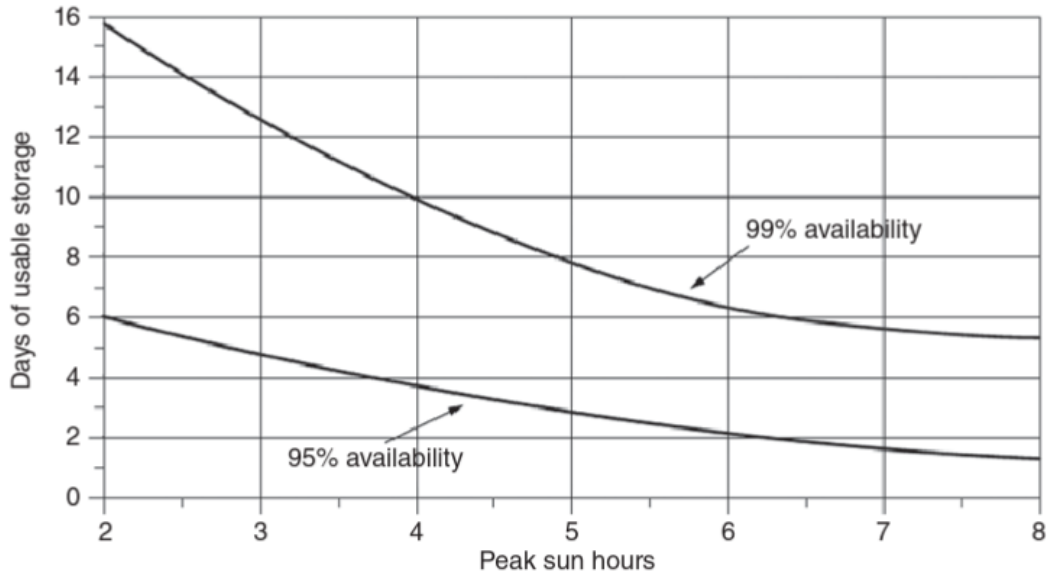


Figure 2.9. Days of battery storage needed for a stand-alone system with 95% and 99% system availability. Peak sun hours are on a month-by-month basis. Based on Sandia Laboratories. Source [36].

The resulting equations that match Figure 2.9 as described in [36], [37] are:

for 99% availability,

$$Autonomy[days] \approx 24.0 - 4.73(PSH) + 0.3(PSH)^2, \quad (2.18)$$

and for 95% availability,

$$Autonomy[days] \approx 9.43 - 1.9(PSH) + 0.11(PSH)^2, \quad (2.19)$$

where the “Peak Sun Hours (PSH) also known as the solar irradiance, is the number of hours per day when the sun intensity is one kilowatt per square meter” [37].

Additionally, the ESS design considers the inverter losses through inverter efficiency, which depends on the load [12]. Most COTS power inverters operate at approximately 90%

efficiency, so 0.9 is used in the first cell of the design tool. In addition to the power loss, the Direct Current (DC) bus voltage must be selected [12]. The DC bus voltage is the battery bank DC input voltage, and the PV array voltage [12], [13]. When selecting the system voltage the author [36] states, “One guideline that can be used to pick the system voltage is based on keeping the maximum steady-state current drawn below 100 A, so that readily available electrical hardware and wire sizes can be used.” Using this as a guideline, the minimum system voltage suggestions are presented in Table 2.1.

Table 2.1. Minimum system voltages based on limiting current to 100 A. Adapted from [36].

Maximum AC Power	Minimum DC System Voltage
<1200 W	12V
1200-2400 W	24 V
2400-4800 W	48 V

To calculate the DC load in kWh/day the expression is depicted as follows,

$$DC_{Load} = \frac{AC_{Load}}{Inverter\ Efficiency}. \quad (2.20)$$

Knowing the system voltage (V_{bus}), the battery bank, as described in [12], will need to supply

$$Load[Ah/day\ at\ DC\ Bus] = \frac{DC_{Load}}{V_{bus}} \quad (2.21)$$

Therefore, the unadjusted battery capacity as described in [12], is expressed as

$$Unadjusted\ Battery\ Capacity[Ah] = Load * Autonomy \quad (2.22)$$

Using the aforementioned design tool, the user at this point can select the type of battery based on the battery specifications programmed into the MS excel document. In the “Battery Specifications” section, the user must know the voltage, capacity, efficiency, the Maximum Depth of Discharge (MDOD), and the battery type and temperature range [13]. Table 2.2 displays the battery characteristics based on model type that are programmed into the excel document developed by [13].

Table 2.2. Models of batteries. Adapted from [12], [13].

Model	Type	Voltage [V]	Capacity [Ah]	Efficiency [%]	MDOD
Trojan SPRE 12 225 [38]	VRLA	12	225	98	80
Trojan 8D-AGM [39]	VRLA	12	230	98	80
SimpliPhi PHI 3.5 [40]	Li-ion	24	138	98	100
Relion RB48V100 [41]	Li-ion	48	100	99	100
Relion RB48V150 [42]	Li-ion	48	150	98	100
Relion RB48V200 [43]	Li-ion	48	200	99	100
Winston LFP400AHA [44]	Li-ion	48	400	98	80
Winston LFP700AHA [45]	Li-ion	48	700	98	80
Winston LFP1000AHC [46]	Li-ion	48	1000	98	80

Temperature is also a major factor in determining a COTS battery source since it affects the overall battery capacity [13]. “A low discharge temperature means a smaller capacity and steeper discharge rate which also causes a decrease in discharge voltage” [47]. However, the battery capacity can be adjusted by the Temperature Correction Factor (TCF) [13]. Temperatures that are greater than 25° C should be kept at 1. “Deep cycle batteries intended for PV systems are often specified in terms of their 20 h or 24 h discharge rate as well as the much longer C/100 rate that is more representative of how they are actually used” [36]. Table 2.3 displays examples of such batteries, including their C/20 rates and various other data [36].

Table 2.3. Example deep-cycle lead-acid battery characteristics. Adapted from [36].

Battery	Electrolyte	Voltage	Nominal (Ah)	Rate (h)	Weight (lbs.)
Rolls Surette 4CS-17P	Flooded	4	546	20	128
Trojan T10S-RE	Flooded	6	225	20	67
Concorde PVX 3050T	AGM	6	305	24	91
Fullriver DC260-12	AGM	12	260	20	172
Trojan 5SHP-GEL	GEL	12	125	20	85

The Ah capacity of a battery not only depends on the rate, but it also depends on temperature [36]. Figure 2.10 is a visual depiction of how temperature affects battery capacity. It compares capacity of different degrees of temperature with the discharge rates to a reference condition of C/20 and 25° C [36]. As shown in Figure 2.10, in colder environments the battery capacity decreases dramatically [36]. Cold temperatures decrease battery capacity, decrease output voltage, and increase vulnerability to the batteries freezing when discharged [36]. Therefore, when operating in cold climates, lead-acid batteries need to be well protected [36].

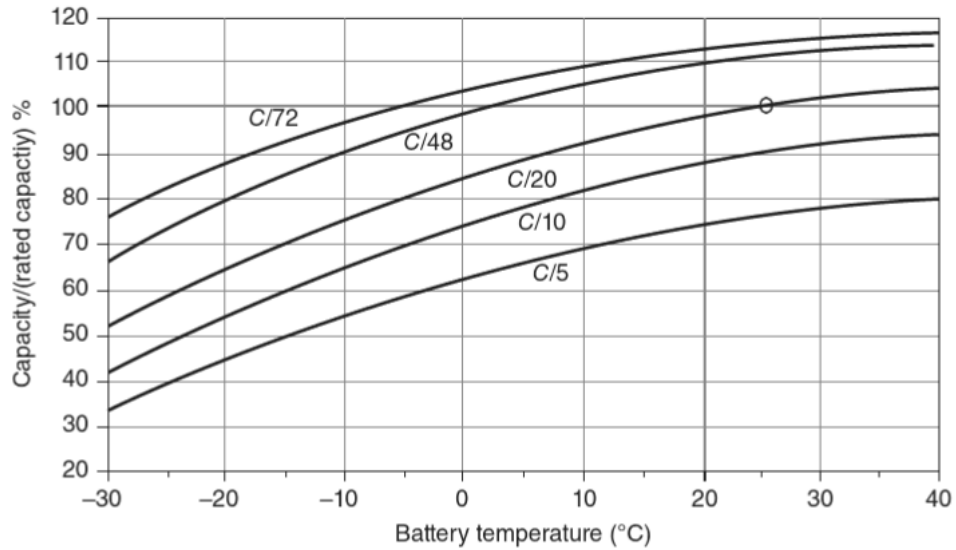


Figure 2.10. Lead-acid battery capacity depends on discharge rate and temperature. The capacity percentage ratio is based on a rated capacity at C/20 and 25°C. Source [36].

The design tool takes into consideration the data from Figure 2.10 and the TCF data identified in Table 2.4 for the different battery types developed by [13]. Additionally, with this design tool, the battery bank system will be properly sized and designed based on user input.

Table 2.4. TCF of lead-acid and Li-ion batteries. Adapted from [12], [13].

Temperature °C	TCF
LA Temp \geq 25	1
LA 25>Temp \geq 20	0.98
LA 20>Temp \geq 15	0.95
LA 15>Temp \geq 10	0.93
LA 10>Temp \geq 5	0.90
LA 5>Temp \geq 0	0.85
LA 0>Temp \geq -5	0.80
LA -5>Temp \geq -10	0.75
LA -10>Temp \geq -15	0.70
LA -15>Temp \geq -20	0.65
Li Temp \geq 5	1
Li 5>Temp \geq 0	0.98
Li 0>Temp \geq -5	0.95
Li -5>Temp \geq -10	0.92
Li -10>Temp \geq -15	0.85
Li -15>Temp \geq -20	0.77

2.4.2 PV Description Sizing

Figure 2.11 displays a generic current-voltage, or “I-V” curve for a PV array. It identifies key parameters to include the open-circuit voltage (V_{OC}) and the short-circuit current (I_{SC}) [36]. Also shown is the power delivered by the module [36]. As observed from the I-V curve, the output power is zero at both ends due to either current or voltage being zero at those points [36]. “The Max Power Point (MPP) is the area near the knee of the I-V curve at which the product of current and voltage reaches its maximum” [36]. The MPPT will monitor the solar panels and determine the MPP voltage for the current conditions. By including a

MPPT we are able to use the simple “peak-hours” approach to system sizing.

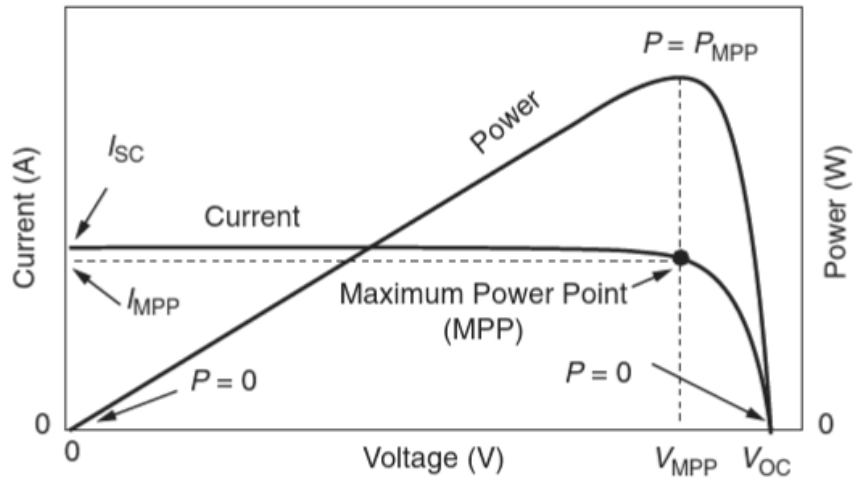


Figure 2.11. PV I-V curve. Source [36].

Figure 2.12 represents a typical solar irradiation profile [12]. The rectangular shaded area under the curve represents the PSH for a solar irradiance of 1 kWh/m^2 .

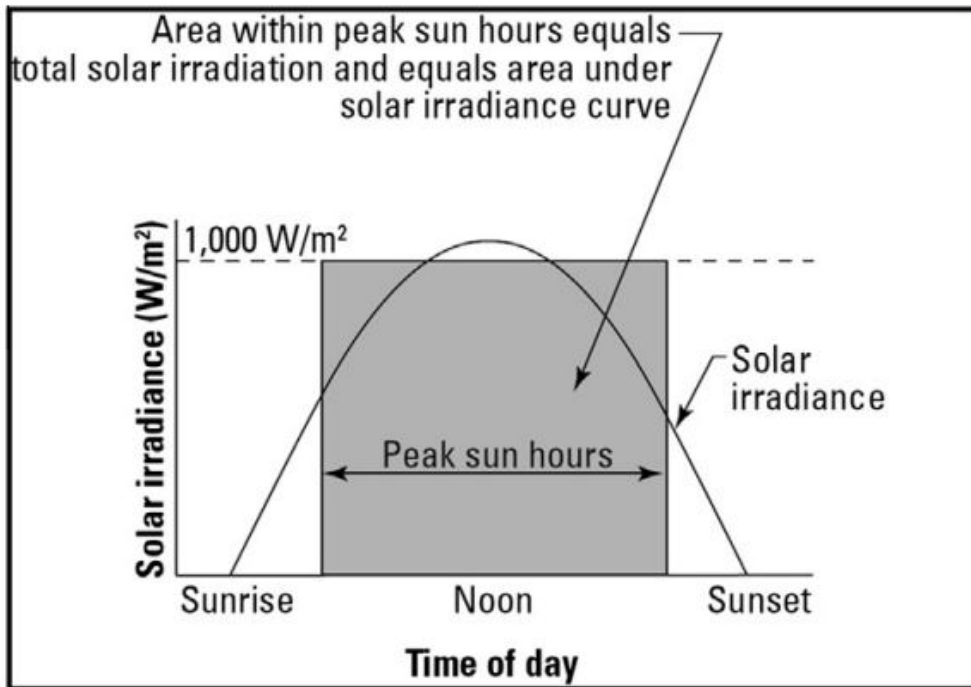


Figure 2.12. Hourly irradiation curve. Source [36].

Without an MPPT the operating point is determined by the intersection of the I-V curve for the batteries with the I-V curve of the PVs [36]. Figure 2.13 shows the daily path of the operating point, which typically will be well below the knee where an MPPT would operate [36]. In this case, the user would lose approximately 20% or so of potential charging power.

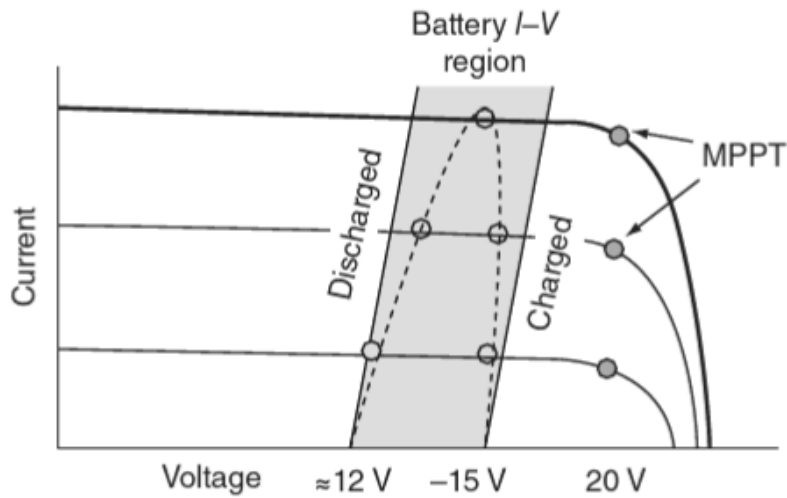


Figure 2.13. I-V curve of PVs with no MPPT. Source [36].

As discussed in [12], [13] the sizing of the PV modules depends largely on the environmental conditions because the solar irradiance and operating temperatures have a significant effect on the performance of the PVs. “Higher temperatures slightly increase the short circuit current, but more drastically decrease the open circuit voltage” [13]. If the short circuit current is directly proportional to the solar irradiance that means the operating voltage is less than the open circuit voltage [13]. The most ideal environments for PV arrays are cool and sunny environments [36]. Using the design tool developed by [13], the MS excel document properly sizes the number of PVs necessary based on when the PVs will be performing at their worst due to increased temperature [13]. The design tool will determine the overall PV design based on user input as shown in Figures 2.6 and 2.7.

CHAPTER 3: MICROGRID CONFIGURATIONS AND RELIABILITY MODELING

This chapter will cover the design of the three microgrid configurations, the associated RBDs, and the system fault trees for each configuration. Additionally, a theoretical reliability estimate analysis will be conducted on each configuration to illustrate how having readily available spare parts and maintenance personnel increases reliability.

3.1 Microgrid Architectures with Varying Numbers of DERs

Different stand-alone microgrid architectures were studied to assess and compare their reliability and resilience. Utilizing COTS DERs including batteries, PV arrays and power converters, three different configurations were designed and assembled in the laboratory.

Each configuration was designed by gradually increasing the number of PV arrays and reconfiguring the battery bank to the required DC voltage input of the inverter. Redundancy was built into the design of the three microgrid configurations to evaluate its impact on the overall reliability of the system.

All three microgrids are mobile, tactical microgrids, assembled with COTS components that can be carried by one individual and can be easily assembled in the field, in support of operations in locations where utility power is not available. The design for each configuration considers the equipment specifications as outlined in Chapter 4.

3.1.1 Microgrid Configuration 1

The stand-alone microgrid system displayed in Figure 3.1 includes three 90 W/35 V PV arrays, each connected to a MPPT through a Single Pole Single Throw (SPST) switch used to cut off power from that specific source when conducting resilience testing as discussed in

Chapter 4. The MPPT solar charge controllers are DC-DC converters with the functionality of battery chargers and they are connected between the PV arrays and the battery bank to regulate the battery charging process. The MPPT enables a PV source to operate at its maximum power point. To ensure the maximum output current of the MPPT is not exceeded, a 50 A circuit breaker was inserted at the output of each MPPT module as an added safety precaution.

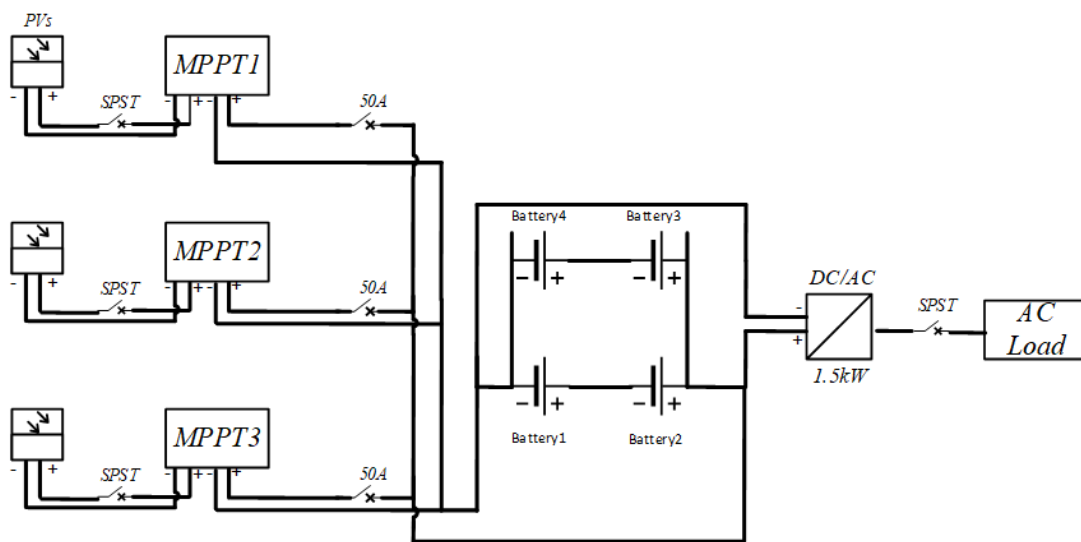


Figure 3.1. Architecture of configuration 1

The MPPTs were placed in parallel with one another due to the ability of the trackers to act as smart controllers and internally determine the total amount of current needed to flow to the batteries based on the overall charge of the battery bank system at any given time. By placing the PVs in parallel, the total current becomes the sum of the currents from each module as shown in Figure 3.2, thus increasing the charge rate to the batteries. Under ideal conditions, Configuration 1 can supply 270 W of solar power to the system.

The 1.5 kW DC-AC power converter, or inverter, requires a 24 V DC input and since each COTS battery module is rated 100 Ah 12 V, a series connection is necessary to provide

24 V at the input of the inverter. Using four 12-V lead-acid batteries, a series and parallel battery bank combination was designed as shown in Figure 3.1. An additional SPST switch was designed into the system as a collection point for the AC data in-between the inverter and the AC load. This specific SPST switch also provides a quick solution to cutting AC power from the inverter for safety reasons.

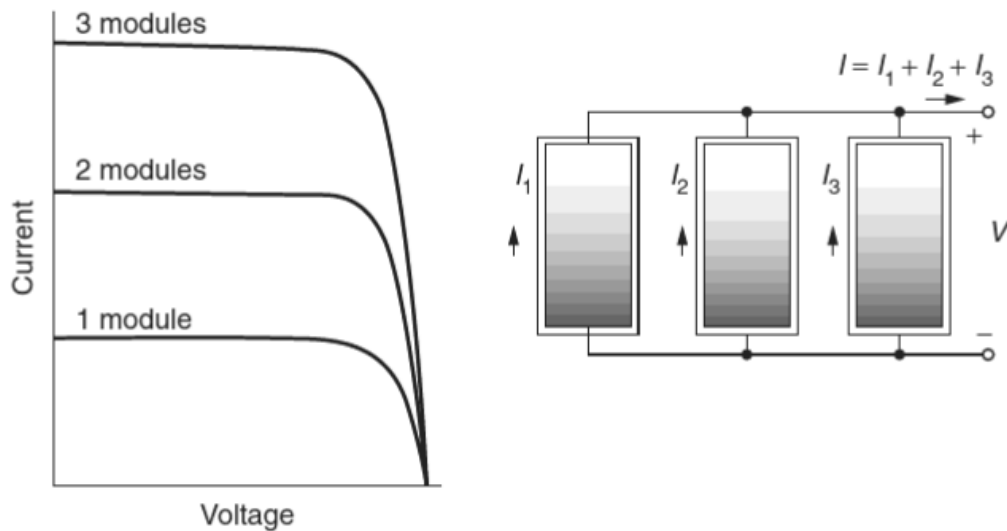


Figure 3.2. Parallel PV arrays, at any given voltage the currents add. Source [36].

3.1.2 Microgrid Configuration 2

The second microgrid configuration displayed in Figure 3.3 differs from the first configuration in the size of the DC-AC inverter, rated 3 kW, and in the addition of a second PV panel at the input of the MPPT3 module. Additionally, since the input of the new inverter is rated at 12 V, the battery bank system was adjusted to a 12 V configuration, where no series connections are necessary for the 12 V battery modules. Three 12-V batteries were placed in parallel and connected to the DC input of the inverter. The fourth battery was kept as a spare part to increase the overall reliability of the system with redundant parts, to be

discussed in Section 3.2.

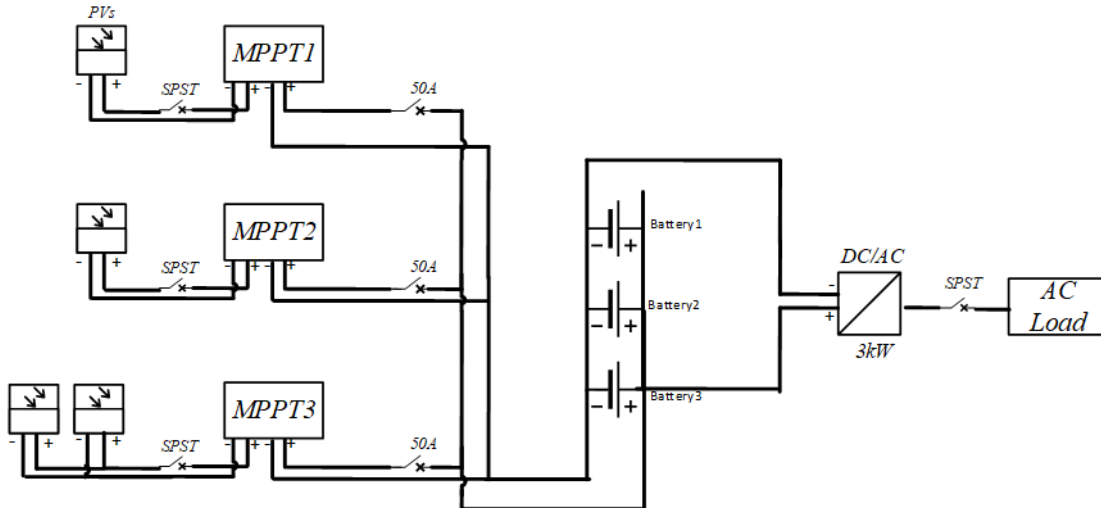


Figure 3.3. Architecture of configuration 2

An additional PV array was added to MPPT3. The two PV arrays were designed to be connected in parallel to MPPT3; this configuration was determined to be the best configuration in order to maximize the output current of the PV arrays connected to MPPT3 as shown in Figure 3.2 for a parallel connection. Additionally, this gives the flexibility for MPPT3 to continue to operate in the event one PV array fails. Under ideal conditions Configuration 2 can theoretically supply 360 W of solar power to the system.

3.1.3 Microgrid Configuration 3

The third configuration is displayed in Figure 3.5 and features an increased number of PV arrays with respect to the previous configurations. The eight PV arrays increase the overall DC power supplied to the microgrid. The three PV arrays connected to MPPT1 and to MPPT2 were connected in parallel rather than in series due to the limited input voltage

rating of the MPPT modules, which is 100 V when the output is 12 V. As shown in Figure 3.4, the series connection of three 42.6 V PV arrays would result in an open circuit voltage of 127.8 V. The max input current of the MPPT controller is 40 A, while at max power the current for each PV array is 2.59 A. When three PV panels are connected in parallel as shown in 3.2, the total output current is 7.77 A, which is well within the max input current of the MPPT controllers. The detailed technical specifications for all the COTS components used in the microgrid testbed are presented in Chapter 4.

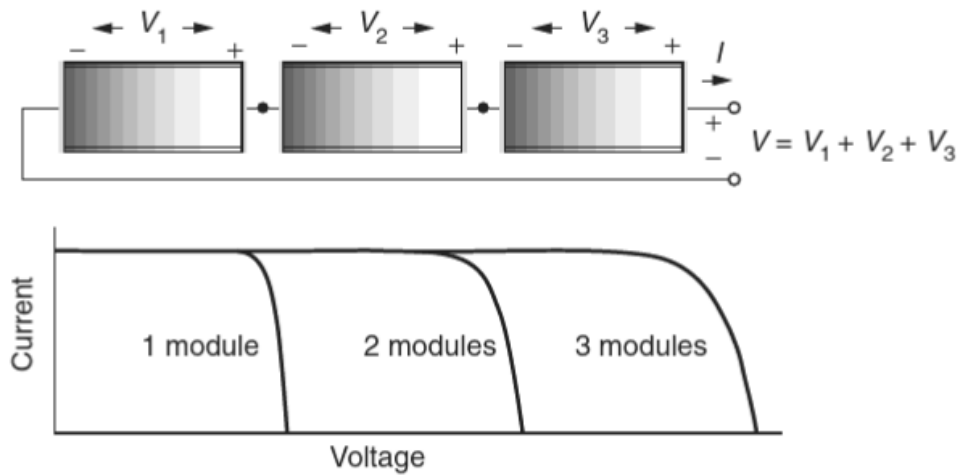


Figure 3.4. Modules in series, at any given current the voltages add. Source [36].

The 3 kW inverter and the 12 V battery bank are left just as they were set up in the second configuration. Under ideal conditions Configuration 3 can supply 720 W of solar power to the system.

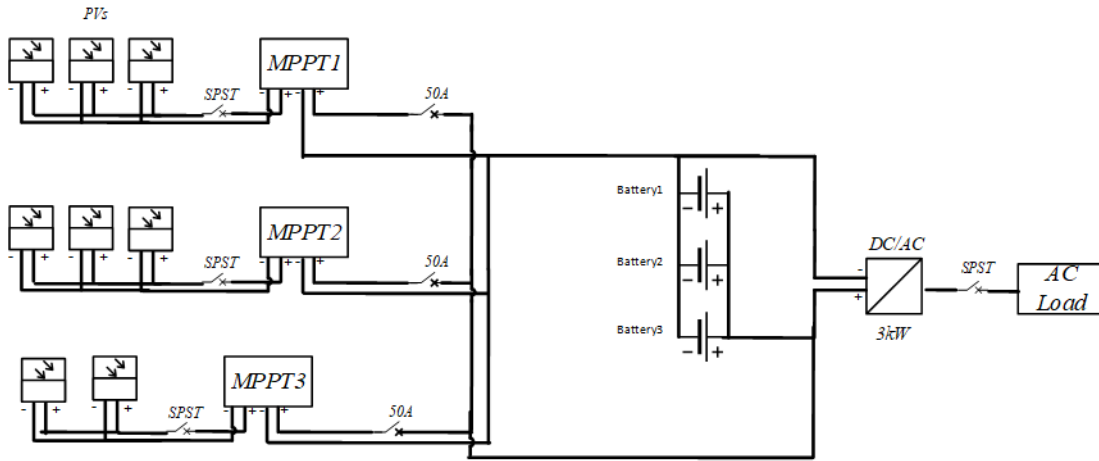


Figure 3.5. Architecture of configuration 3

3.1.4 Reliability Block Diagram for Configuration 1

The design for each configuration includes an RBD to analyze the overall component relationship of the system. Wires were not included in the reliability analysis of each configuration due to failure of the wires being an order of magnitude lower than the components identified in the models [15]. The RBD displayed in Figure 3.6 identifies the key components of the stand-alone microgrid and shows the component relationship in a combined series and parallel manner used for conducting reliability analysis. Using the architecture from Figure 3.1, each PV array is connected in series with its respective MPPT. Each serial PV array and MPPT is then connected in parallel. In each parallel branch, all components are identical and will continue to function in the event a series component is not working. The second branch, comprising of the 24 V battery bank system, was placed in a series and parallel combination to meet the DC voltage requirement of the inverter. The second branch is then connected to the inverter. The batteries are designed to have a full state of charge prior to each experiment. The environment plays a factor in the overall reliability analysis as it has a significant impact on the PV arrays and could impact the

batteries and inverter depending on geographical location and where they are placed. The mathematical approach below takes into consideration that the reliability values of specific components are identical – that is all PV arrays, MPPTs, and the batteries (BATTs) are of the same model and brand, and therefore their reliability is assumed to be identical.

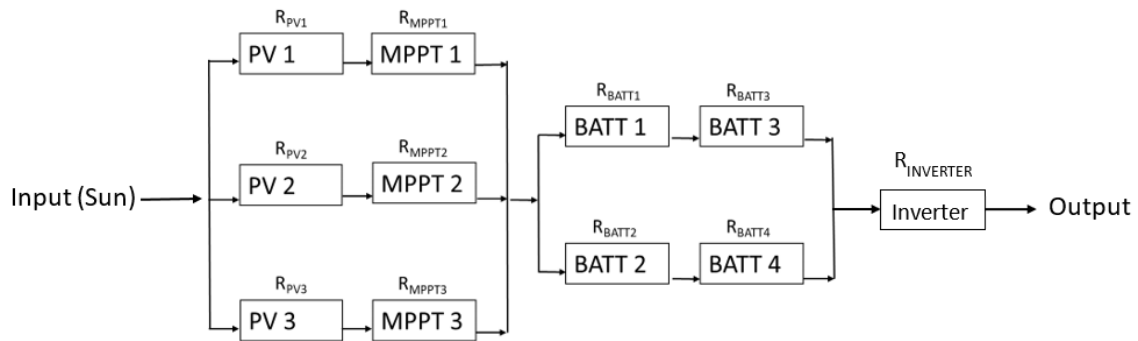


Figure 3.6. RBD for microgrid configuration 1

In analyzing the series network in Figure 3.6, each subsystem PV-MPPT and BATT-BATT, the reliability of that specific component is the product of the components in series and is expressed as

$$R_{PM} = (R_{PV})(R_{MPPT}) \quad (3.1)$$

and

$$R_{BATT1} = (R_{BATT})(R_{BATT}). \quad (3.2)$$

In analyzing the parallel network given that each component is identical, the reliability expression for the 3 component system is

$$R_A = 1 - (1 - R_{PM1})(1 - R_{PM2})(1 - R_{PM3}) = 1 - (1 - R_{PM})^3. \quad (3.3)$$

For the 2 component parallel system reliability is expressed as

$$R_B = R_{BATT1} + R_{BATT2} - (R_{BATT1})(R_{BATT2}). \quad (3.4)$$

Therefore, the combined series-parallel network can be expressed as

$$R_{Config1} = [1 - (1 - R_{PM})^3][R_{BATT1} + R_{BATT2} - (R_{BATT1})(R_{BATT2})][R_{INV}]. \quad (3.5)$$

3.1.5 System Fault Tree Configuration 1

Figure 3.7 displays the system fault tree for the first microgrid configuration where the system at the top-level of the diagram represents the stand-alone microgrid. Flowing down the tree using an OR *logic gate*, system failure will occur if at least one of the three events occur: failure of the inverter, failure of the battery bank, or failure of the entire PV array system. Over any given time the AND *logic gate* at the battery bank system requires failure of both series connection for the entire system to fail. Given each battery bank series connection is 24 V, that is sufficient for the entire system. Additionally, at any given time the AND *logic gate* at the PV array system requires all three connections to fail to cause an overall system failure. Redundancy was built into the system through the battery bank system and the PV arrays. As show in Figure 3.7, depending on the AC power output of the inverter, the load can still support the mission duration with half of the battery bank system and one-third to two-thirds of the PV array system.

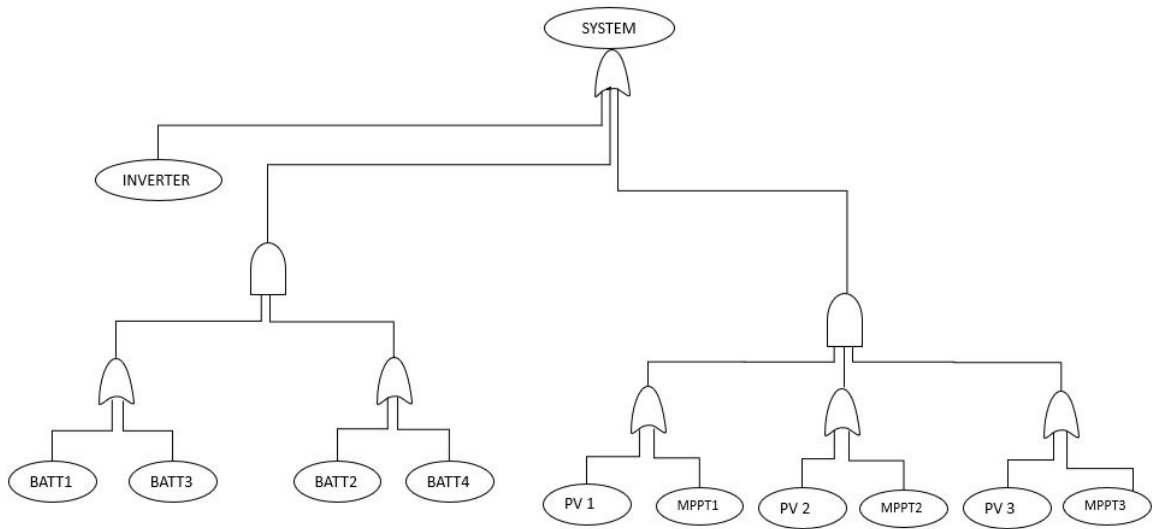


Figure 3.7. System fault tree for microgrid configuration 1

Figure 3.8 shows how reliability of the overall system can be increased with readily available spare parts. Using the equations from Section 3.3, mathematically we will see a slight increase in the overall reliability of the system with an increase in number of spares available within a specific timeframe.

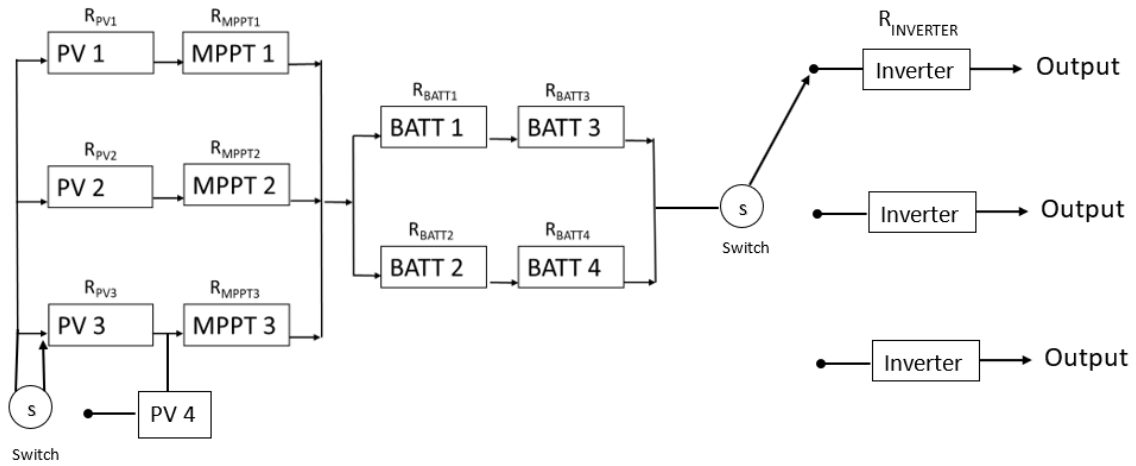


Figure 3.8. Microgrid configuration 1 reliability diagram with spares readily available

3.1.6 Reliability Block Diagram for Configuration 2

Similar to Figure 3.6, the RBD displayed in Figure 3.9 shows the component relationship of the entire system for configuration 2. The key differences between the two configurations are the added PV array to MPPT3 and the three 12-V parallel battery bank system.

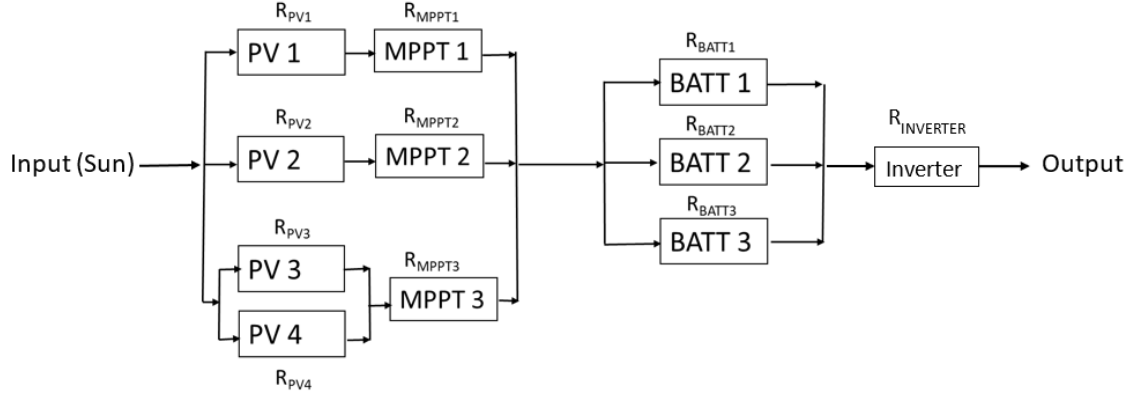


Figure 3.9. RBD for microgrid configuration 2

In analyzing the reliability of the entire system, the reliability for parallel connection of PV3 and PV4 can be expressed as

$$R_{PV34} = R_{PV3} + R_{PV4} - (R_{PV3})(R_{PV4}). \quad (3.6)$$

Furthermore, the series connection of R_{PV34} and R_{MPPT3} can be expressed as

$$R_{PM3} = (R_{PV34})(R_{MPPT3}). \quad (3.7)$$

Therefore, the overall reliability can be expressed as

$$R_{Config2} = [1 - (1 - R_{PM1})(1 - R_{PM2})(1 - R_{PM3})][1 - (1 - R_{BATT})^3][R_{INV}]. \quad (3.8)$$

3.1.7 System Fault Tree for Configuration 2

Similar to Figure 3.7, the fault tree depicted in Figure 3.10 indicates system failure when a single one of three items fails: the inverter, the entire battery bank system, or the PV array system. The battery bank system requires all batteries to fail to cause a system level failure. Furthermore, the PV array system requires either a PV array or MPPT controller to fail in each of the three trains to cause a failure of that subsystem. With an extra PV array on the third train, both PV arrays or the MPPT has to fail to cause a failure of that subsystem.

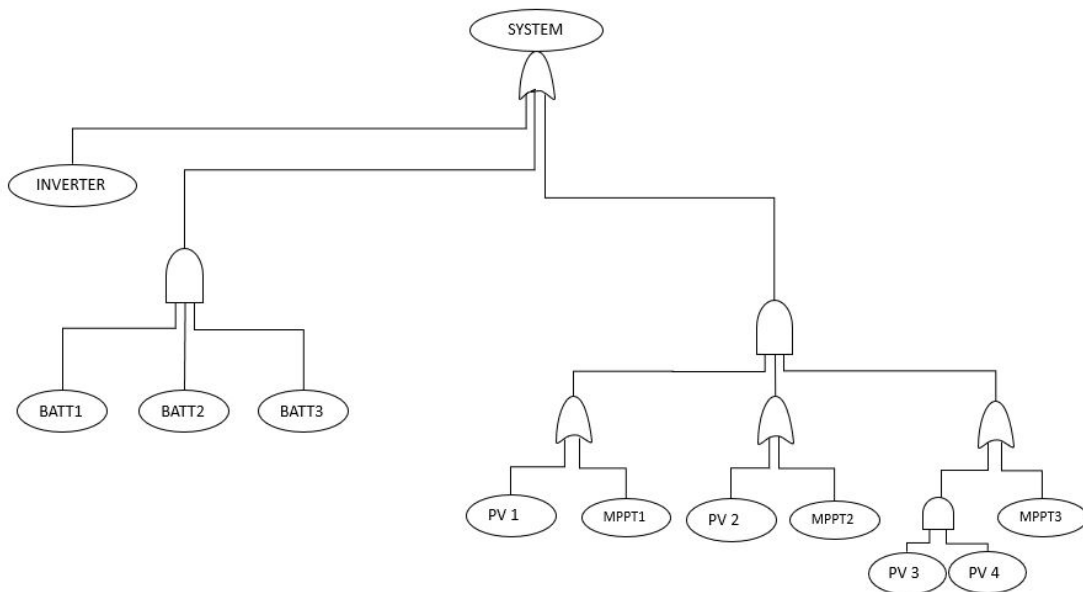


Figure 3.10. System fault tree for microgrid configuration 2

Figure 3.11 shows how reliability of the overall system can be increased with readily available spare parts. Similar to Configuration 1, we will see an increase in the overall reliability of the system with an increase in number of spares available within a specific timeframe.

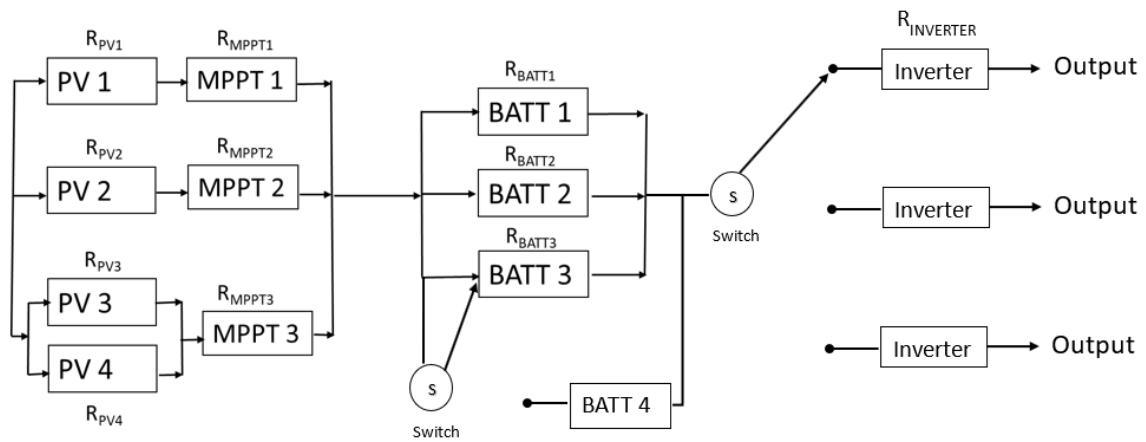


Figure 3.11. Microgrid configuration 2 reliability diagram with spares readily available

3.1.8 Reliability Block Diagram for Configuration 3

The RBD displayed in Figure 3.12 shows the component relationship of Configuration 3. Similar to Configurations 1 and 2, the reliability expression for each component can be expressed in mathematical terms identified below. Reliability is increased with the added PV arrays.

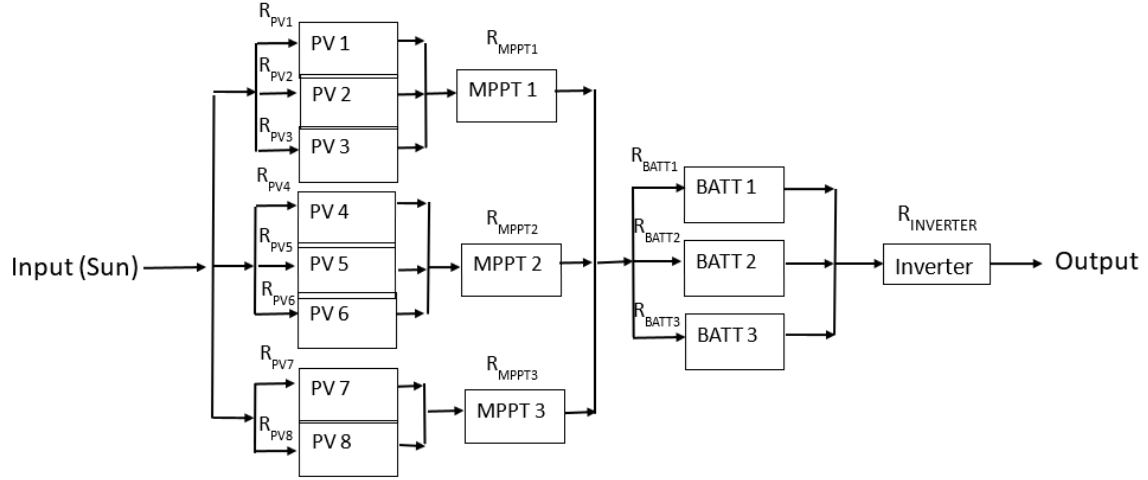


Figure 3.12. RBD for microgrid configuration 3

The reliability expression for the parallel connection given all components are identical for PV1, PV2, and PV3 is

$$R_{PV123} = 1 - (1 - R_{PV1})(1 - R_{PV2})(1 - R_{PV3}) = 1 - (1 - R_{PV})^3. \quad (3.9)$$

Thus the series combination of R_{PV123} and R_{MPPT1} can be expressed as

$$R_{PM1} = (R_{PV123})(R_{MPPT1}). \quad (3.10)$$

The reliability expression for the parallel connection given all components are identical for PV4, PV5, and PV6 is

$$R_{PV456} = 1 - (1 - R_{PV4})(1 - R_{PV5})(1 - R_{PV6}) = 1 - (1 - R_{PV})^3. \quad (3.11)$$

Thus the series combination of R_{PV456} and R_{MPPT2} can be expressed as

$$R_{PM2} = (R_{PV456})(R_{MPPT2}). \quad (3.12)$$

The parallel combination of R_{PV7} and R_{PV8} can be expressed as

$$R_{PV78} = R_{PV7} + R_{PV8} - (R_{PV7})(R_{PV8}). \quad (3.13)$$

The resulting series combination of R_{PV78} and R_{MPPT3} can be expressed as

$$R_{PM3} = (R_{PV78})(R_{MPPT3}). \quad (3.14)$$

Therefore the overall reliability can be expressed as

$$R_{Config3} = [1 - (1 - R_{PM1})(1 - R_{PM2})(1 - R_{PM3})][1 - (1 - R_{BATT})^3][R_{INV}]. \quad (3.15)$$

3.1.9 System Fault Tree for Configuration 3

Similar to the previous fault trees, the fault tree for Configuration 3 in Figure 3.13 shows that the system level failure remains the same as Configurations 1 and 2. Figure 3.13 shows the probability of failure is significantly reduced with the addition of the extra PV arrays.

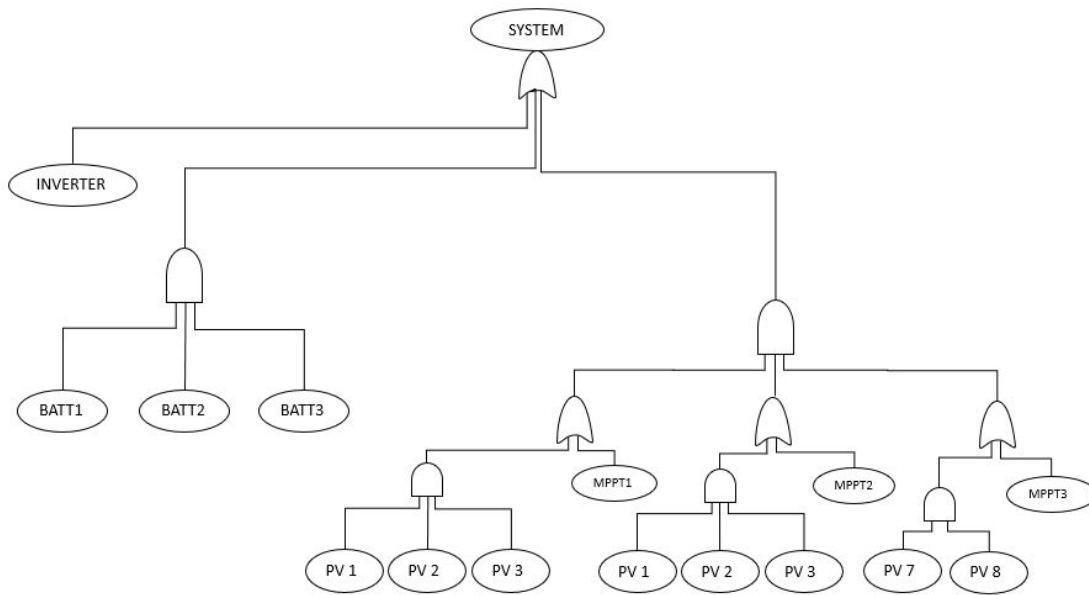


Figure 3.13. System fault tree for microgrid configuration 3

Figure 3.14 shows how reliability of the overall system can be increased with readily available spare parts. As discussed in the previous configuration, we will see an increase in the overall reliability of the system with an increase in number of spares available within a specific timeframe. Multiple spare parts and personnel were readily available to perform maintenance on the system, which increases the overall reliability of the stand-alone microgrid.

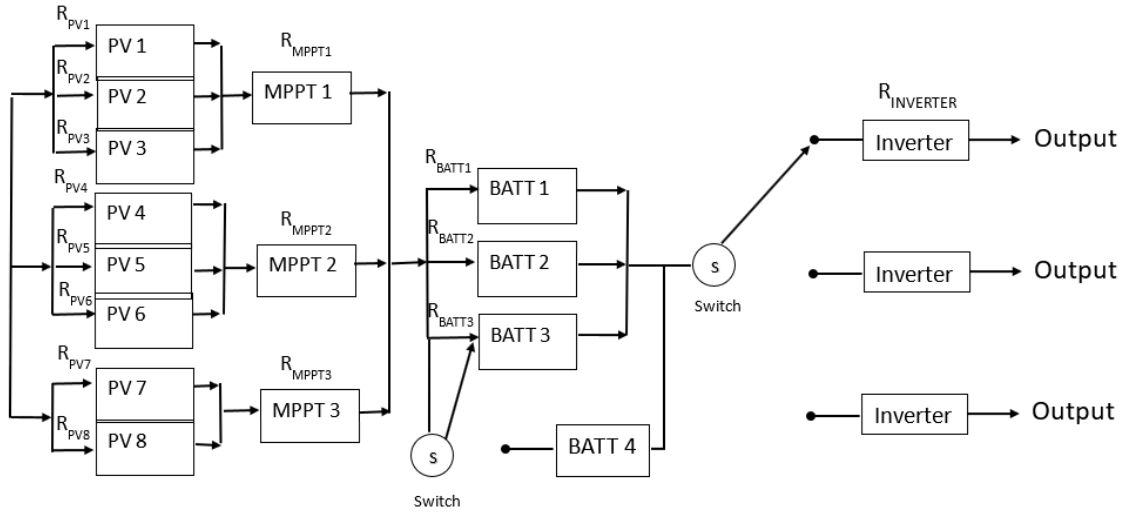


Figure 3.14. Microgrid configuration 3 reliability diagram with spares readily available

3.2 Increasing Reliability with Spare Parts

The probability of success of a system to complete its mission can be increased with the availability of spare parts. To determine the probability that a system has not failed with readily available spare parts, given that failures can occur randomly and are exponentially distributed as described in [30] can be expressed as

$$P = e^{-\lambda t} + (\lambda t)e^{-\lambda t}. \quad (3.16)$$

The probability of success given x number of spares available within a given time t can be simplified into Poisson expression as described in [30] as

$$f(x) = \frac{(\lambda t)^x e^{-\lambda t}}{x!}. \quad (3.17)$$

Increasing reliability of the system with spare parts does not include the downtime or ready time of the system while specific parts are being replaced. To determine the availability of the system to include the mean maintenance downtime will require the use of the operational availability equation as discussed in Section 2.2.

3.3 Reliability Estimate and Comparison of the Three Configurations

In order to estimate the reliability of the microgrid configurations, the reliability of each component was determined using the theoretical value of 0.95 with a failure rate of 0.05 for each key component listed in the RBDs for each configuration. Utilizing the reliability equations presented in Section 2.2, reliability can be determined for each configuration utilizing the equations obtained from the RBD analysis. The computations below show a quantitative analysis for reliability as well as show an increase in the reliability of the system with readily available spare parts.

For Configuration 1, the reliability expression becomes:

$$R(t) = 1 - F(t) = 1 - (0.05) = 0.95 \quad (3.18)$$

$$R_{PM} = (R_{PV})(R_{MPPT}) = (0.95)(0.95) = 0.9025 \quad (3.19)$$

$$R_{BATT1} = (R_{BATT})(R_{BATT}) = (0.95)(0.95) = 0.9025. \quad (3.20)$$

Using equation (3.5), the overall reliability is

$$R_{Config1} = [1 - (1 - 0.9025)^3][0.9025 + 0.9025 - (0.9025)(0.9025)][0.95] = \mathbf{0.9401}.$$

The theoretical instantaneous failure rate λ for each configuration using equation (3.16) to

solve for λ replacing P with each theoretical reliability value is

$$\lambda_1 = \mathbf{0.3580}, \lambda_2 = \mathbf{0.3252}, \lambda_3 = \mathbf{0.3238}. \quad (3.21)$$

Using the exponential distribution function, the probability of success given 1 spare is available and can be replaced within 1.1 hours using equation (3.16) with $x=1$ and $t=1.1$ is

$$P_1 = \mathbf{0.9401}, P_2 = \mathbf{0.9494}, P_3 = \mathbf{0.9498}. \quad (3.22)$$

The probability of success given two spares are available and can be replaced at the same time using equation (3.17) with $x=2$ and $t=1.1$ is

$$f(x)_1 = 0.0523, f(x)_2 = 0.04474, f(x)_3 = 0.04442. \quad (3.23)$$

Therefore, the probability of success becomes $1-f(x)$

$$P2_1 = 1 - f(x)_1 = \mathbf{0.9477}, P2_2 = 1 - f(x)_2 = \mathbf{0.9553}, P2_3 = 1 - f(x)_3 = \mathbf{0.9556}. \quad (3.24)$$

Table 3.1 captures the overall increase in theoretical reliability with readily available spare parts using the equations outlined in Section 3.2 for each configuration. We notice that the reliability of the system increases with the availability of spare parts. However, the spare parts analysis does not account for the downtime and various availability parameters as previously discussed. Another important note is that these values can fluctuate based on the availability of the spare part and the time it takes to replace them.

Table 3.1. Theoretical probability of success with spares available for each configuration

Configuration	R(t)	λ	1 spare within 1.1 hrs.	2 spares replaced at the same time within 1.1 hrs.
1	0.9401	0.3580	0.9401	0.9477
2	0.9494	0.3252	0.9494	0.9553
3	0.9498	0.3238	0.9498	0.9556

CHAPTER 4: EXPERIMENTAL MEASUREMENTS AND RESULTS

This chapter presents the experimental setup and the outcome of the stand-alone microgrid experiments for the microgrid configurations discussed in Chapter 3. The goal of the experiments is to evaluate the time to failure of each microgrid configuration and how the different configurations perform with respect to each other.

4.1 Experimental Microgrid Set-up

A microgrid testbed was setup in the laboratory to perform resilience testing on the three different microgrid configurations described in Chapter 3. This section presents the main COTS components used to assemble the stand-alone microgrid and the measuring instruments used to collect the experimental data. A notional block diagram of the stand-alone microgrid is displayed in Figure 4.1 and it shows the key elements used in the experimental testbed.

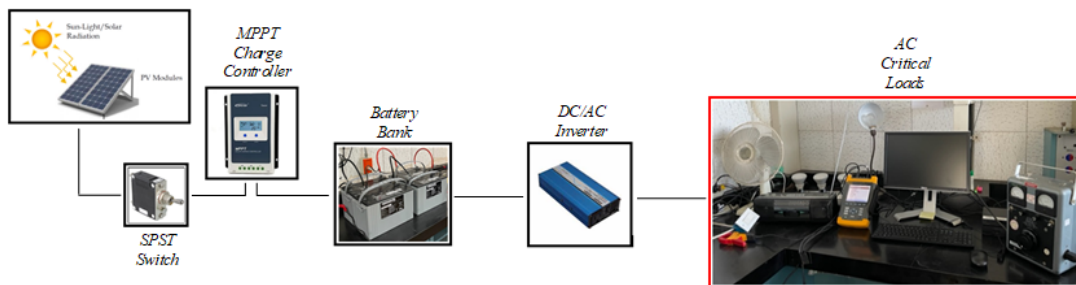


Figure 4.1. Notional block diagram of the experimental setup, each configuration consists of varying amount of PVs and Batteries

4.1.1 Microgrid COTS components

This section presents and discusses the following COTS components used to assemble the three experimental microgrid configurations for the resilience experiments:

- PV panels
- MPPT modules
- lead-acid batteries
- circuit breakers
- DC-AC converters (inverters)

The PV panels are Solartech arrays with a maximum power rating of 90 W each and include 36 high efficiency polycrystalline solar cells per panel [48]. The detailed specifications are listed in Table 4.1 and a photograph is shown in Figure 4.2

Table 4.1. Specification of the PV arrays used in experiment. Adapted from [48].

Manufacturer	Solartech Power, Inc.
Model Number	SPM090P
Rated Maximum Power (P_{max})	90 W
Current at P_{max} (I_{mp})	2.59 A
Voltage at P_{max} (V_{mp})	35.0 V
Short-Circuit Current (I_{sc})	2.72 A
Open-Circuit Voltage (V_{oc})	42.6 V
Solar Cells	36 cells in a 4x17 matrix connected in series



Figure 4.2. Solartech PV array. Source [48].

The MPPT modules are EPEVER Tracer4210AN MPPT Solar Charge Controllers each of which consist of a DC-DC converter that regulates the charge of the battery bank, and can quickly track the maximum power point of the PV arrays and obtain the maximum power output from the PV arrays under any conditions. There are several different battery voltage control parameters within the MPPT modules based on the battery type and battery voltage that the user can modify. The battery voltage control parameters selected for the experiments were the lead-acid sealed parameters for the 12 V battery bank system and those values were doubled for the 24 V battery bank as per instructions in the user manual [49]. Communication of the modules is primarily through the MT50 remote meter which displays various operating data and system level faults. The remote meter is an extension of the MPPT module that allows the user to visually display data through the Liquid Crystal Display (LCD) screen about the system or adjust system parameters as needed [49]. The detailed specifications are listed in Table 4.2 and a photograph is shown in Figure 4.3

Table 4.2. Specification of the tracer4210 MPPT solar charge controller used in experiment. Adapted from [49].

Manufacturer	EPEVER
Model Number	Tracer4210AN
Battery compatibility	Sealed (default) Gel Flooded Lead-acid batteries
Rated Charge Current	40 A
Rated Charge Power	520 W/12 VDC 1040 W/24 VDC
Max. PV input current (I_{input})	40 A
Max. PV Open-Circuit Voltage (V_{oc})	100 V/12 VDC 92 V/24 VDC
Solar Cells	36 cells in a 4x17 matrix connected in series



Figure 4.3. Tracer4210AN MPPT solar charge controller. Source [49].

The batteries used in the experimental setup are lead-acid 12 V 100 AH Deep Cycle AGM and uses 200 cycles at 80% discharge with the specifications outlined in Table 4.3 and a photograph shown in Figure 4.4 [50].

Table 4.3. Specification of the 12 V 100 AH deep cycle AGM. battery. Adapted from [50].

Manufacturer	Werker
Model Number	WKDC12-100PUS
Voltage	12 V
Lead-Acid Type	Deep Cycle
Capacity	100 AH
Product Category	Sealed Lead-Acid



Figure 4.4. 12 V 100 AH deep cycle AGM battery. Source [50].

The SPST switches used in the experimental setup are circuit breaker magnetic (hydraulic delay) 30 A 80 V DC toggle panel mount switches manufactured by Sensata-Airpax, part number 723-1400-ND. The specifications for the circuit breaker are listed in Table 4.4 and a photograph is shown in Figure 4.5.

Table 4.4. Specification of the circuit breaker magnetic-hydraulic lever. Adapted from [51].

Manufacturer	Sensata-Airpax
Voltage Rating - DC	80 V
Current Rating	30 A
Actuator Type	Toggle
Number of Poles	1



Figure 4.5. Circuit breaker magnetic-hydraulic lever. Source [51].

A key element of the microgrid is the DC-AC power converter, or inverter, which converts the DC voltage at the output of the batteries to the AC voltage required by the loads. Two inverters were used in the three microgrid configurations: one rated 1500 W and the other rated 3000 W. Both DC-AC converters used in the experimental setup are manufactured by AIMS Power and their specifications are outlined in Table 4.5. Photographs of the inverters are shown in Figure 4.6.

Table 4.5. Specification of the DC-AC power inverters. Adapted from [52], [53].

Manufacturer	AIMS Power
Model	PWRI150024S PWRI300012120S
DC Input Voltage	24V (19-32V) 12V (9.8-16V)
Output Power	1500W 3000W
Efficiency	>90%
Battery Low Alarm	DC $19.6 \pm .5V$ DC $9.8 \pm .3V$
Battery Low Shutdown	DC $19 \pm 1V$ DC $9.5 \pm .5V$



(a) 1500W



(b) 3000W

Figure 4.6. DC to AC Power Inverters. Adapted from [52], [53].

The AC critical load consisted of several items obtained from the laboratory. A list of items and power consumption details are listed in Table 4.6. The metered variac and the space

heater were connected to serve as an AC variable load up to 1.5 kW. When the metered variac and space heater were powered together, that adjusted power was not considered a part of the critical load. A photograph of the load is shown in Figure 4.7. When all items were connected, the measuring instrument displayed 222 W of AC power consumed due to the internal resolution of the instrument. The AC critical load was established as the baseline AC power consumption required to achieve mission success.

Table 4.6. AC critical load description

Devices	AC Power Consumption	Time	Total Energy
Sony CFS-220 radio	12 W	24 h	288 Wh
Desk Fan	48 W	24 h	1152 Wh
LED Lights	36 W	24 h	864 Wh
Halogen Lamp	72 W	24 h	1728 Wh
Vivo Mini V66 Mini PC	24 W	24 h	576 Wh
Dell 19" LCD Monitor	48 W	24 h	1152 Wh
Metered Variac Autotransformer and Space Heater	12 W	24 h	288 Wh
JBL-GO Wireless Bluetooth Speaker	12 W	24h	288 Wh
Total	264 W	24 h	6336 Wh

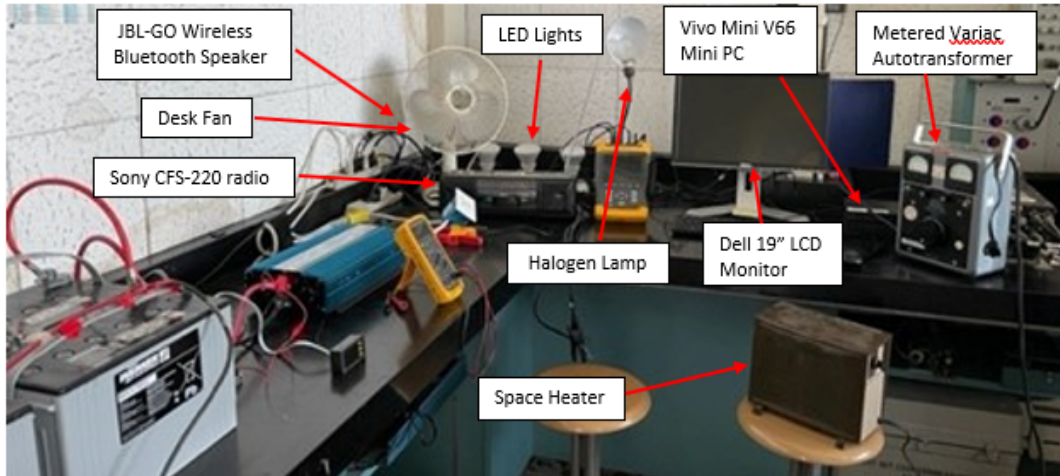
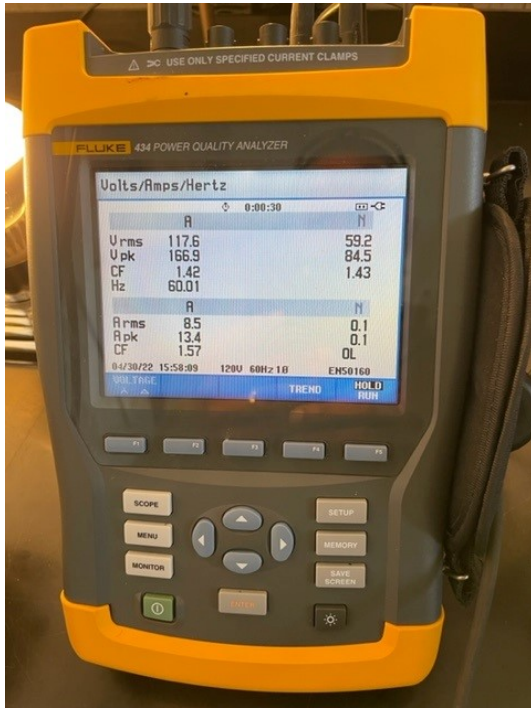


Figure 4.7. AC critical load display

4.1.2 Measurement Instruments

The microgrid testbed includes some measuring instruments necessary to the data collection during the experimental tests. A Fluke 434 Power Quality Analyzer was used as the primary source of data collection. There are multiple channels that can be used to capture data based on the wiring configuration of the Fluke 434. The $1\emptyset$ +Neutral is a single phase with neutral wire setting that is viewed in Channel A in Figure 4.8 (a) [54]. The $1\emptyset$ Split Phase wire setting is a split phase configuration that displays two channels, Channel A and Channel B as shown in Figure 4.8 (b) [54]. For configurations 1 and 2, the $1\emptyset$ +Neutral setting was used and Channel A collected the AC data as shown in Figure 4.8 (a). Configuration 3 used the $1\emptyset$ Split Phase wire setting; Channel A collected the AC data while Channel B collected the DC voltage only. The Fluke 434 power quality analyzer is designed to collect only AC data, however, it was determined that the DC voltage of the system could be captured and recorded as well. The third configuration utilized the Fluke 434 voltage meter to capture the DC voltage along with AC data.



(a) Channel A



(b) Channel A and B

Figure 4.8. Fluke 434 power quality analyzer

The settings of the Fluke 434 used during the experiment are displayed in Table 4.7. All data captured by the Fluke 434 was collected using the powerlog software in [55], which captured data in real time. “The Fluke PowerLog allows users to download recorded data from the Fluke 434 Power Quality Analyzer to a workstation” [55]. The software also provides users with the ability to generate data tables and graphs and to export data to other programs [54], [55].

Table 4.7. Fluke 434 settings

Configurations	1Ø +Neutral 1Ø Split Phase
Frequency	60 Hz
Nominal Voltage	120 V
Voltage Ratio	1:1
Current Ratio	1:1

The MPPT Solar Charge Controllers captured the current and voltage at the output of the PV arrays and at the input of the batteries. All data captured was displayed by the MT50 remote meters directly connected to the MPPT modules. Photographs of the MT50 meters and their setup on the microgrid testbed are shown in Figure 4.9. The MT50 remote meters are a visual display of the voltage and current of both the PV arrays and the batteries and also show the battery state of charge levels at any given time. The 24 V battery voltage control parameters for the MPPT were used as previously discussed [49]. A 7-in-1 bidirectional volt amp meter DC 0-90 V 300 A, part number 200536FBA, was used to monitor the DC voltage and current at the input to the power inverter as shown in Figure 4.10.



(a) MT50 Remote Meter



(b) MT50 Remote Meters and MPPT SCCs

Figure 4.9. MT50 remote meters and MPPT solar charge controllers



Figure 4.10. Bidirectional volt/amp meter

4.2 Experimental Measurements

All experiments were conducted in Monterey, California from April to June 2022. The average solar radiation for the three months is approximately $6.2 \text{ kWh/m}^2/\text{day}$ based on the

graph shown in Figure 4.11. Figure 4.12 depicts a solar map of the United States showing the estimated PV power potential daily and yearly.



Figure 4.11. Solar radiation data in Monterey, CA. Source [56].

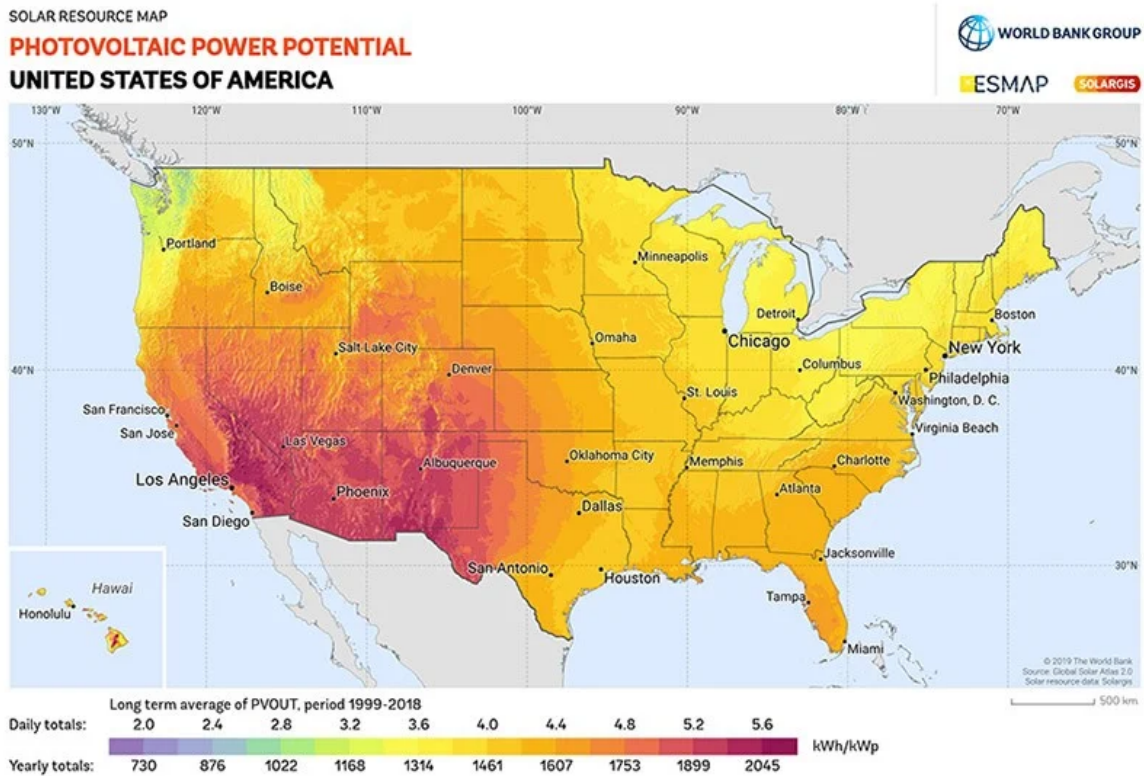


Figure 4.12. PV Power Potential in the United States of America. Source [57].

Several non-destructive experiments were conducted in the laboratory to observe the performance of the three microgrid configurations when various faults were simulated, such as failure of a solar panel or other key component. The goal is to compare the resilience of the three configurations by analyzing how the system and its components adapt to the changing environment and its ability to recover from those disruptive events [10]. Additionally, reliability of the system was tested through back-to-back experiments to determine the probability of success for each subcomponent.

A total of forty-four different experiments were conducted increasing and decreasing the AC power consumed to observe how the three microgrid configurations respond when a fault is simulated. The experiments aim to assess the time between the occurrence of a simulated fault and the failure of the system, where failure is defined as the unavailability of sufficient power for the critical load. This relates to the mission success, as it is defined as the ability of the microgrid to service AC critical loads for the entire duration of a military operation. In this case, providing enough energy to sustain operations throughout a 15-hour work day. In the field, a normal workday is 12-hours, however, for leadership the workday is extended due to debriefs, planning, and refining products for the next day. That could take anywhere from 2-3 additional hours which is why 15 hours is listed.

The experiments were performed on the three microgrid configurations with several electrical loads functioning as the AC critical load established as the baseline AC power consumption required to achieve mission success. The critical load includes the AC devices listed in Table 4.6 and shown in Figure 4.7. During the experimental testing the AC power consumption was increased in increments beyond the established baseline AC power consumption until the maximum rated power of the inverter was reached. Each AC power increment was tested multiple times and ran until the system failed in order to obtain the average operating times. The goal was to test the reliability and resilience of the overall system in order to determine mission success when operating at various power consumption.

All components with the exception of the PV arrays were indoors under ideal indoor temperatures for Monterey County at approximately 86 feet above sea level [58]. The desk fan was utilized as an added cooling source for the power inverter to prevent overheating. Once the power inverter reached the undervoltage limit as stated in Table 4.5, it shut off and the batteries had to be recharged.

4.2.1 Resilience Experiments with Configuration 1

Sixteen different experiments took place over 16 days, both day and night for microgrid Configuration 1. The baseline AC critical load consumed approximately 200 W of AC power and did not include the Light-Emitting Diode (LED) lights and the halogen lamp during testing due to availability of gear at the time. Table 4.8 displays the experimental parameters for Configuration 1, including power consumption, total time to failure of the system, and the peak solar irradiance for that day.

Table 4.8. Experimental data for configuration 1

Test	AC Power Consumption	Time to Failure	Peak Solar Irradiance
Day 1	1513 W	1.33 h	1101 W/m ²
Night 1	1513 W	1.22 h	
Day 2	1513 W	1.33 h	513 W/m ²
Night 2	1513 W	1.03 h	
Day 3	1513 W	1.35 h	1013 W/m ²
Night 3	1513 W	1.03 h	
Day 4	1513 W	1.42 h	1108 W/m ²
Night 4	1513 W	1.17 h	
5	200 W (AC Critical Load)	21.1 h	956 W/m ²
6	330 W	8.33 h	1118 W/m ²
Day 7	710 W	3.38 h	970 W/m ²
Night 7	710 W	2.7 h	
Day 8	1080 W	2 h	1110.2 W/m ²
Night 8	1080 W	1.78 h	
Day 9	1513 W	1.13 h	1090 W/m ²
Night 9	1513 W	1.07 h	
10	200 W (AC Critical Load)	19.12 h	1060 W/m ²
11	330 W	8.4 h	1049 W/m ²
Day 12	710 W	3.72 h	1028 W/m ²
Night 12	710 W	2.08 h	
Day 13	1080 W	2.55 h	1117 W/m ²
Night 13	1080 W	1.63 h	
Day 14	1513 W	1.33 h	1015 W/m ²
Night 14	1513 W	1.07 h	
15	Varied	10.72 h	968 W/m ²
16	Varied	12.38 h	413 W/m ²

All plots were similar with different variations in the time to failure of the system. Figures 4.13 - 4.15 display the experimental plots created with Matlab using the exported data from the Fluke PowerLog software for Test 10, while the load was drawing 200 W as shown in Table 4.8. Figures 4.13 and 4.14 display the Root Mean Square (RMS) voltage and current as well as the power measured at the load. The spikes in Figures 4.14 and 4.15 were due to moving the computer mouse to wake the computer up. We also notice the AC voltage, current, and power all begin to drop around 18.78 hours into the experiment and goes to zero after 19.12 hours of operating. After sunset, the microgrid was able to support the critical load for a total of 9.35 hours. The amount of power supplied by the PV arrays for that particular day was approximately the same as the power drawn by the load, therefore, the load was not supported by the microgrid indefinitely due to incorrect sizing of the critical load. However, the load was able to meet mission success and supply enough power to support a 15-hour work day. The system powered off after the power inverter reached the undervoltage limit of 19 V as indicated in Table 4.5 for the 24-V battery bank system. This indicates that the critical load should be reduced at night in order to sustain operations throughout the night with Configuration 1 and the operating conditions of Test 10 from Table 4.8.

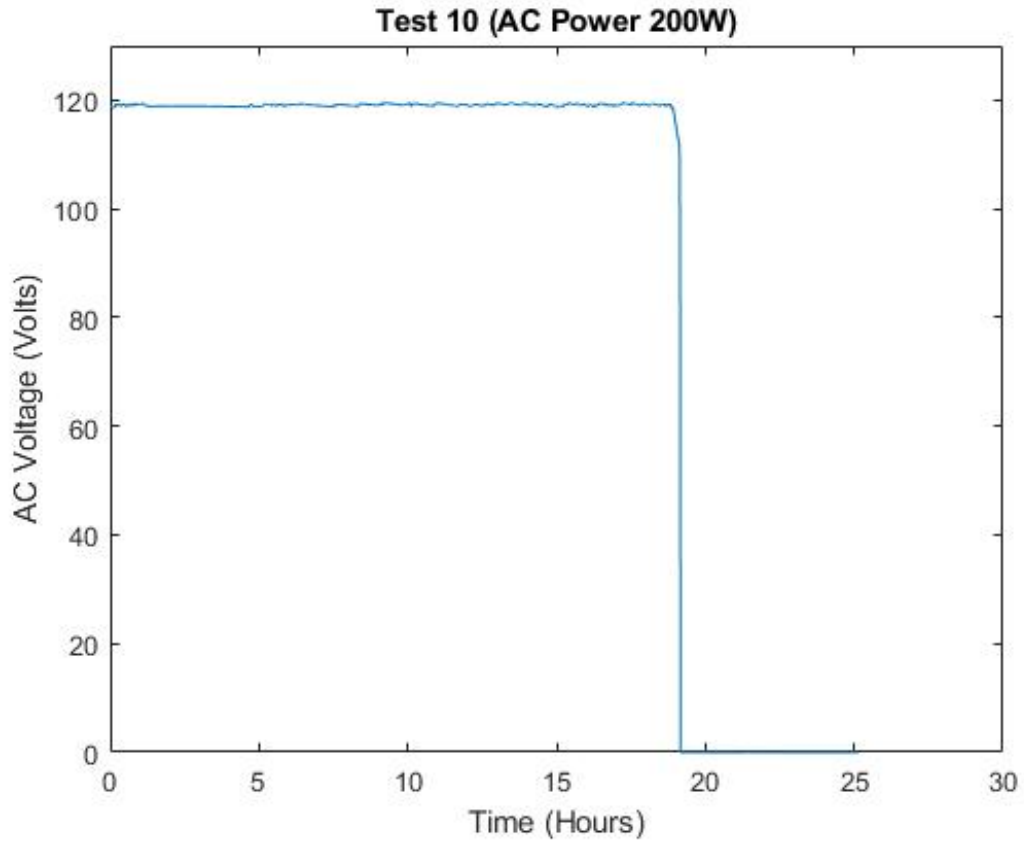


Figure 4.13. Experimental voltage plot for test 10 (AC power increment 200 W)

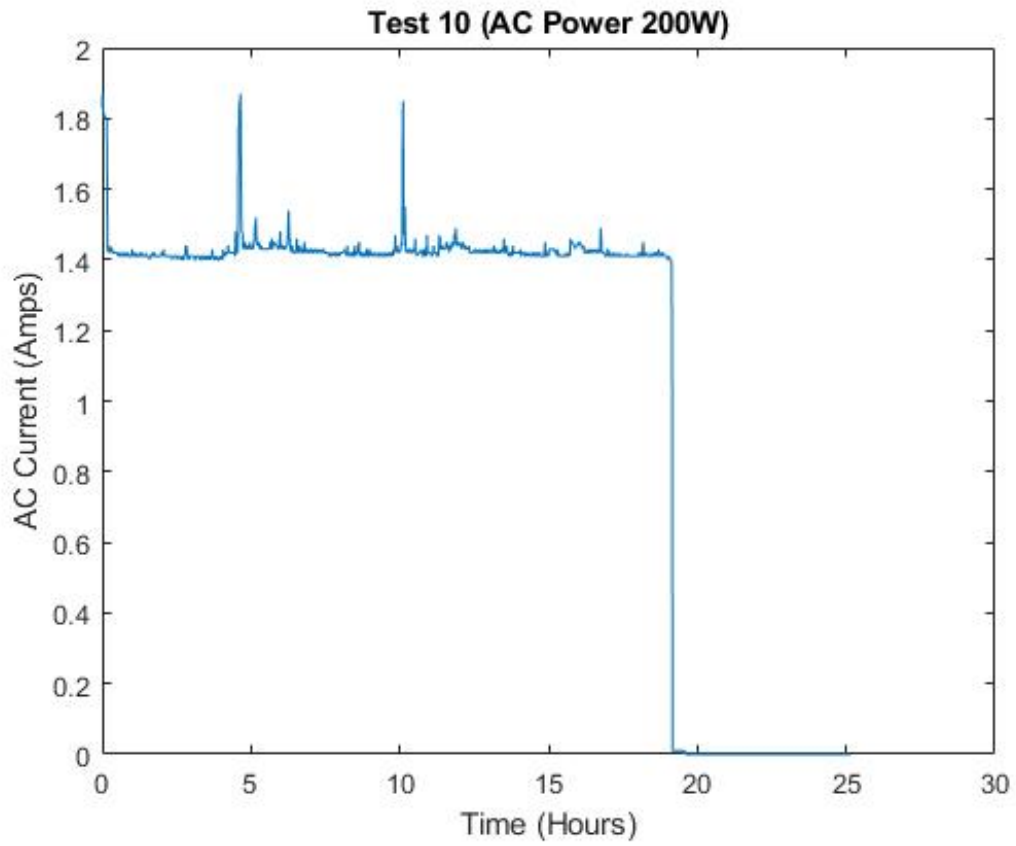


Figure 4.14. Experimental current plot for test 10 (AC power increment 200 W)

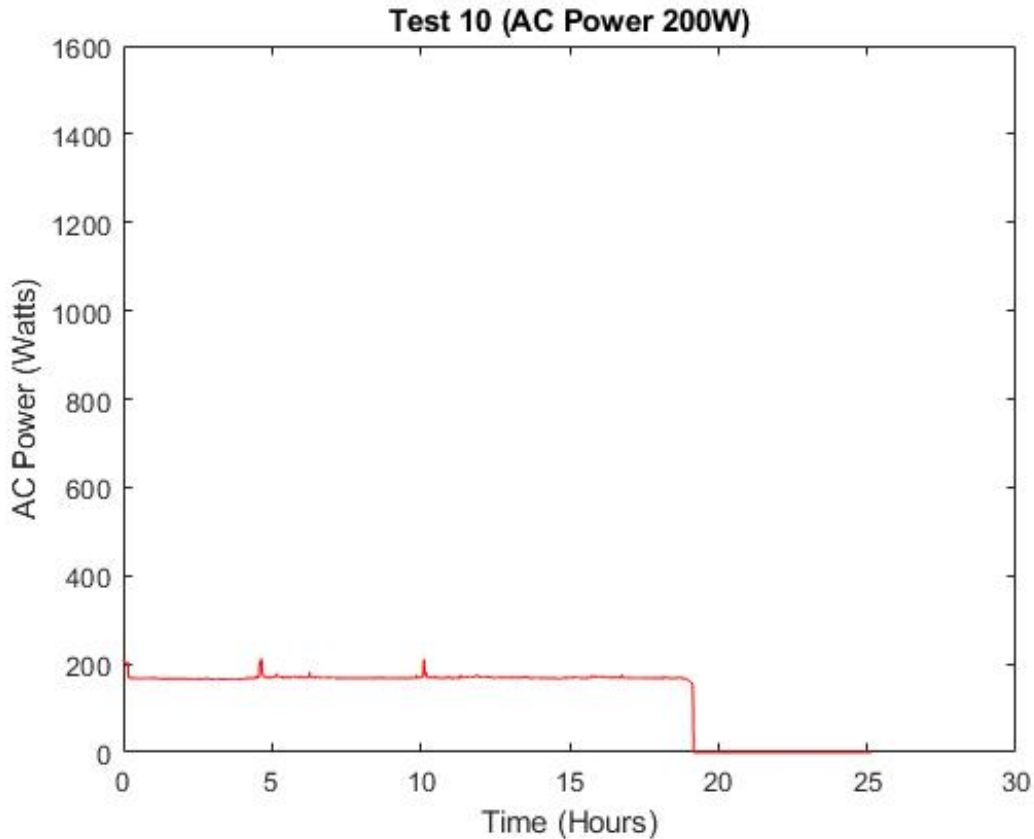


Figure 4.15. Experimental power plot for test 10 (AC power increment 200 W)

Tests 15 and 16 of Table 4.8 executed a stress test, which consisted of a series of steps designed to see how the system responds to its changing environment and its ability to recover from disruptive events. The steps are described here:

- A portion of the PV arrays were covered for one hour to simulate solar obstruction of the panels,
- Each SPST switch was turned off in one-hour increments for a total of 3 hours until no solar power was supplied to the system to simulate failure of that PV array subsystem,
- The AC power supplied to the system was stepped up to the maximum power consumption of 1513 W and was held for 15 consecutive minutes of an hour to simulate power fluctuation,

- The test concluded by turning back on the SPST switches and reducing the AC power to the 200 W baseline power consumption after 3 hours of testing.

After the conclusion of the stress test, the system remained on at the baseline power consumption until the power inverter shut off due to reaching the undervoltage limit. Figures 4.16 - 4.18 display the results obtained from Test 16 of the stress test as shown in Table 4.8.

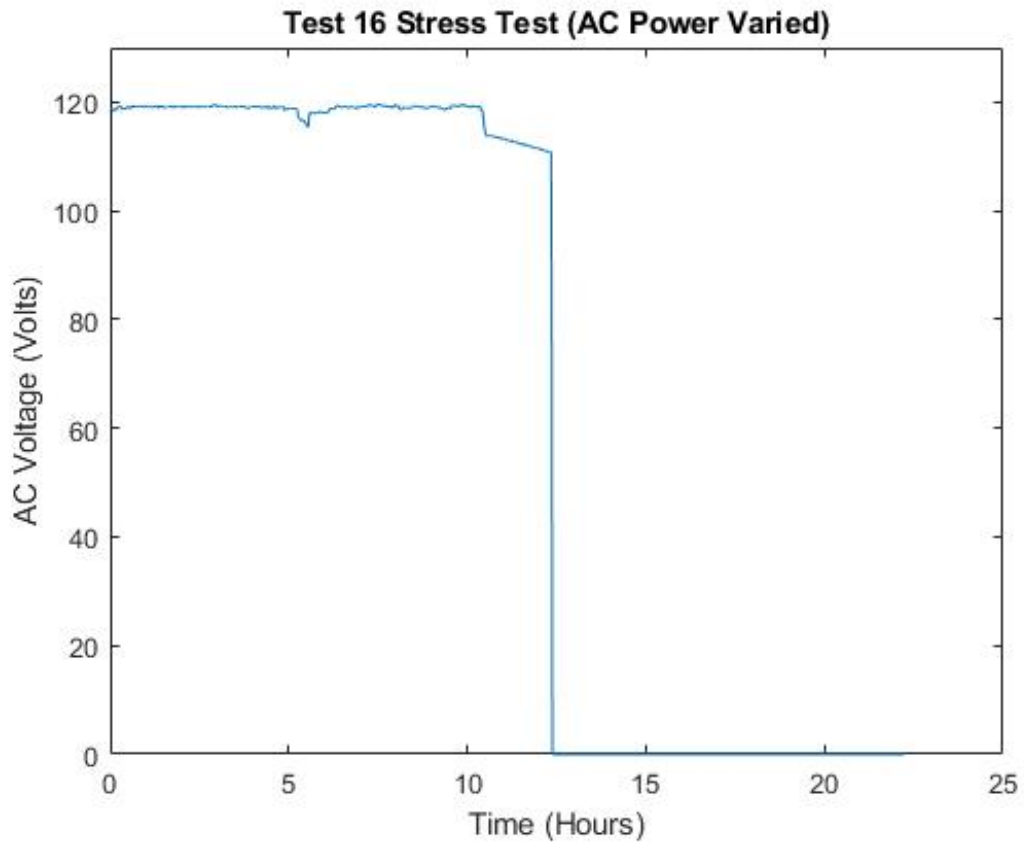


Figure 4.16. Experimental voltage plot for the stress test

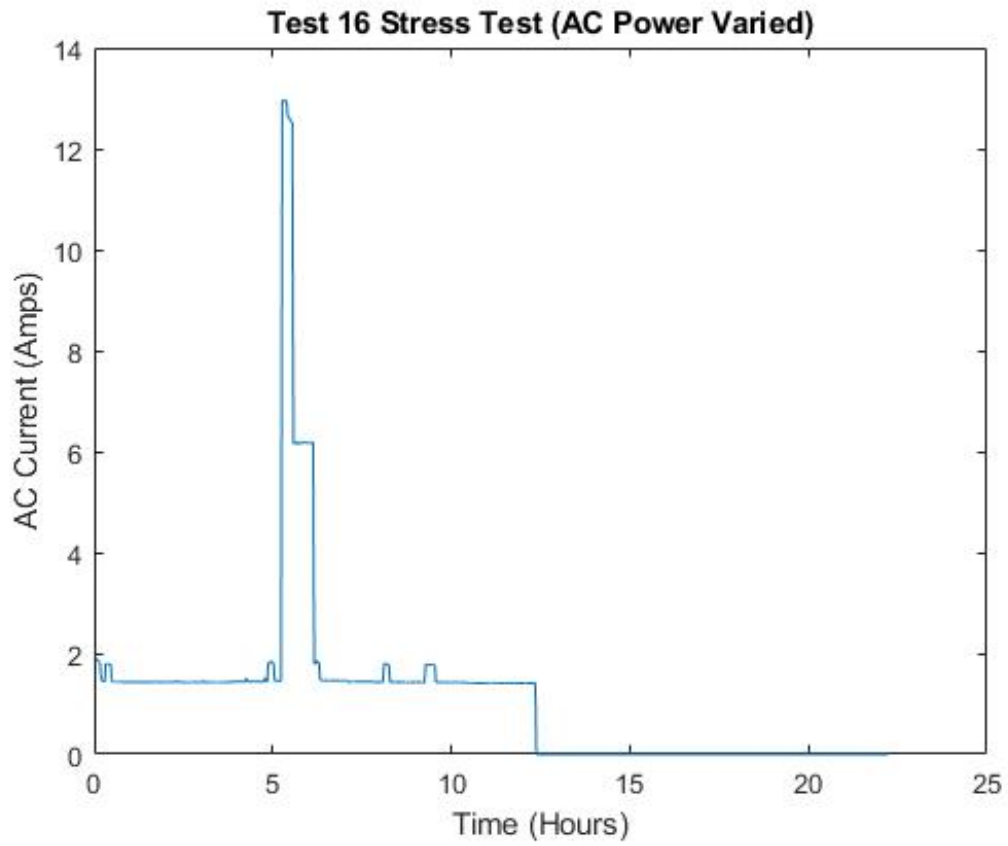


Figure 4.17. Experimental current plot for the stress test

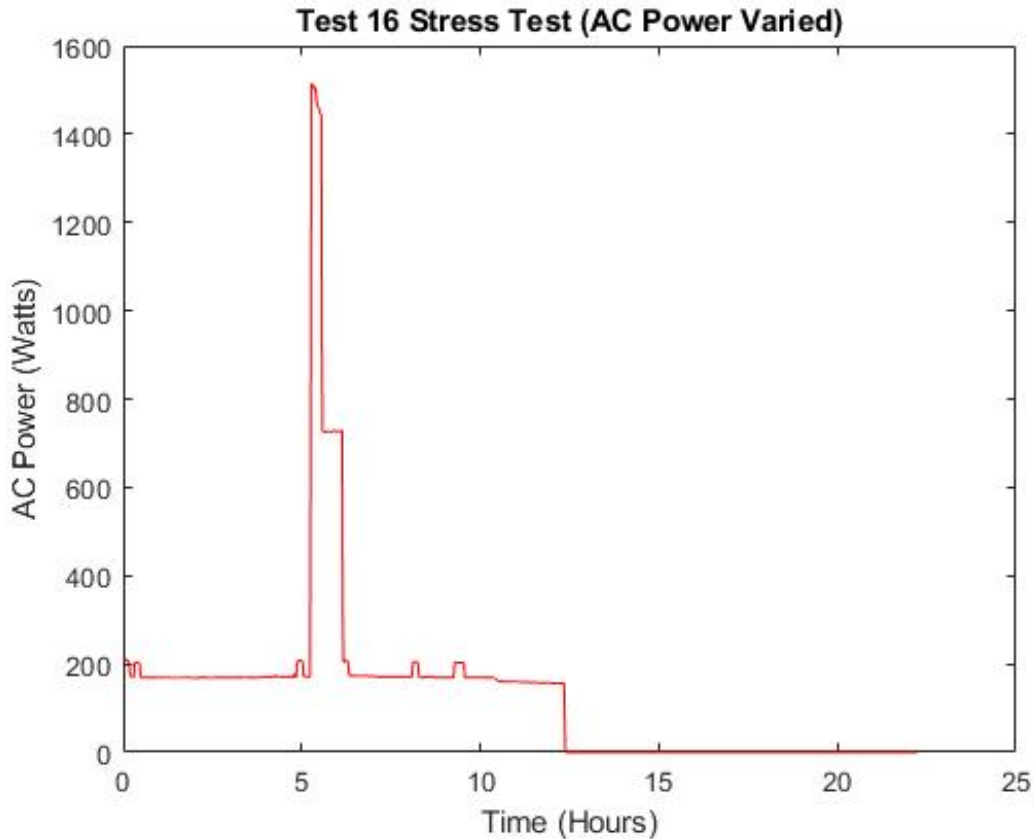


Figure 4.18. Experimental power plot for the stress test

Throughout the 16 different experiments conducted for Configuration 1, no components failed randomly, the system became unavailable when the batteries were depleted. When failure was not simulated, all components operated nominally and were functional when called upon to work. Once the batteries were recharged, the microgrid was operational and ready for use. Equation (4.1) shows the number of hours it would take to recharge the batteries at the charging current rate for Configuration 1 using only the supplied solar energy. The total charging current was approximately 8 A. After depleting the batteries multiple times and recharging using only solar energy, it was observed that it would take 2 days to recharge the batteries to a full state of charge.

$$\text{Battery charging time (h)} = \frac{C_{batt}}{I_{supplied}} = \frac{100 \text{ Ah}}{8 \text{ A}} = \mathbf{12.5 \text{ h.}} \quad (4.1)$$

With the use of a rechargeable battery source, the BK precision high power programmable DC power supplies model XLN3640 plugged into 120 AC mains power, the batteries would charge in approximately 3 hours. The settings of the rechargeable battery source were set to 24 V and 35 A. Equation (4.2) shows the time it would take to recharge the batteries with the added rechargeable source. This significantly reduced the recharging time of the battery bank.

$$\text{Battery charging time (h)} = \frac{C_{batt}}{I_{supplied}} = \frac{100 \text{ Ah}}{35 \text{ A}} = \mathbf{2.86 \text{ h.}} \quad (4.2)$$

The total operating time for each test in Configuration 1 is 114 hours, and the number of failures/stoppages of the system was 21.

4.2.2 Resilience Experiments with Configuration 2

Eight different experiments (tests 17 - 24) were conducted on microgrid Configuration 2 and resulted in the data listed in Table 4.9. Initially, the baseline AC critical load was tested. Then the AC variable load was used to increase the power consumption to continue with reliability and resilience testing of the system. The added PV array contributed to the increase in the overall solar power; however, the 3-kW power inverter and the 12-V battery bank system pulled a larger amount of DC current (double that of the previous configuration) to support each AC power consumption. This resulted in lower total operating time of the system. The 3-kW inverter with the 12-V battery bank for the baseline power consumption (the AC critical load) was drawing approximately 20 A of DC current. Whereas the 1.5-kW inverter with the 24-V battery bank for the baseline power consumption (the AC critical load) was drawing approximately 9.5 A of DC current.

Table 4.9. Experimental data for configuration 2

Test	AC Power Consumption	Time to Failure	Peak Solar Irradiance
17	222 W (AC Critical Load)	15.5 h	1027 W/m ²
18	607.95 W	2.63 h	1022 W/m ²
19	1198.5 W	1.33 h	997 W/m ²
20	1722.16 W	0.9 h	1030 W/m ²
21	Varied	6.68 h	1015 W/m ²
22	222 W (AC Critical Load)	16.65 h	1024 W/m ²
23	607.95 W	3.12 h	1077 W/m ²
24	Varied	8.73 h	935 W/m ²

For the 3-kW power inverter, the maximum power consumption that was tested was 1.7 kW due to the system not lasting more than an hour under higher power loads. Figures 4.19 - 4.21 from Test 20 show a gradual decrease over time until the power inverter shut off at 0.9 hours of operating at 1.7 kW of AC power. This power consumption was operating at 57% of the inverter power rating.

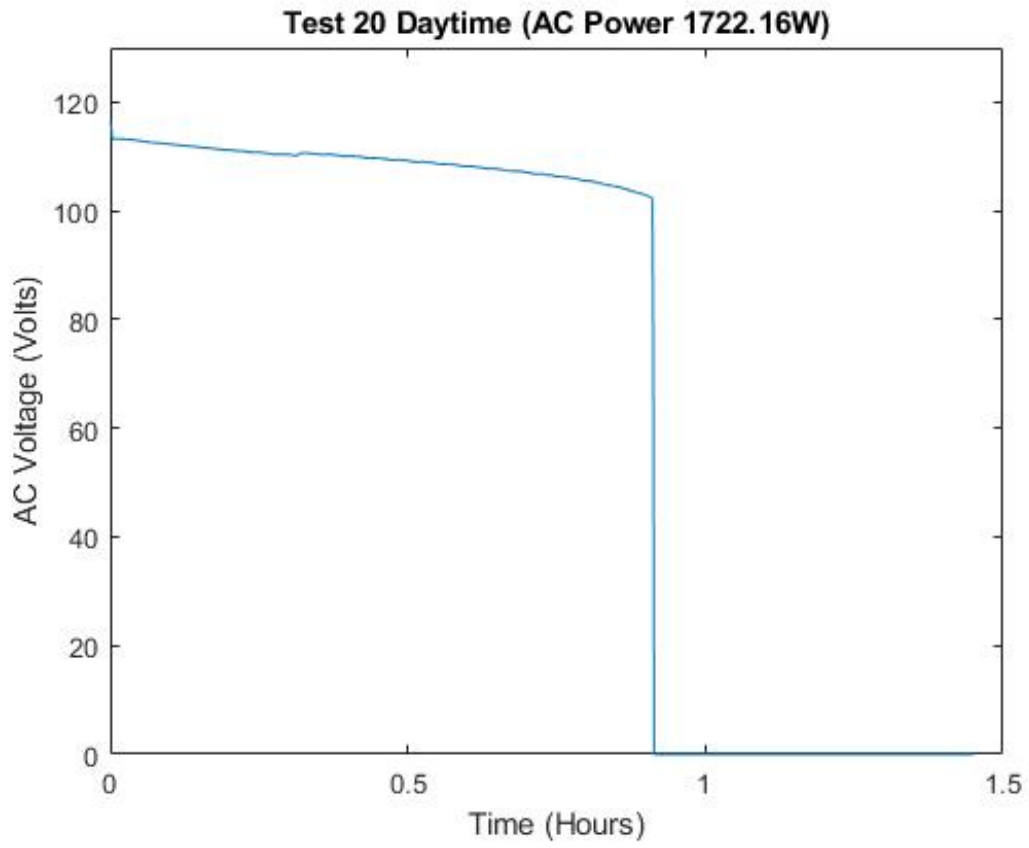


Figure 4.19. Experimental voltage plot for test 20

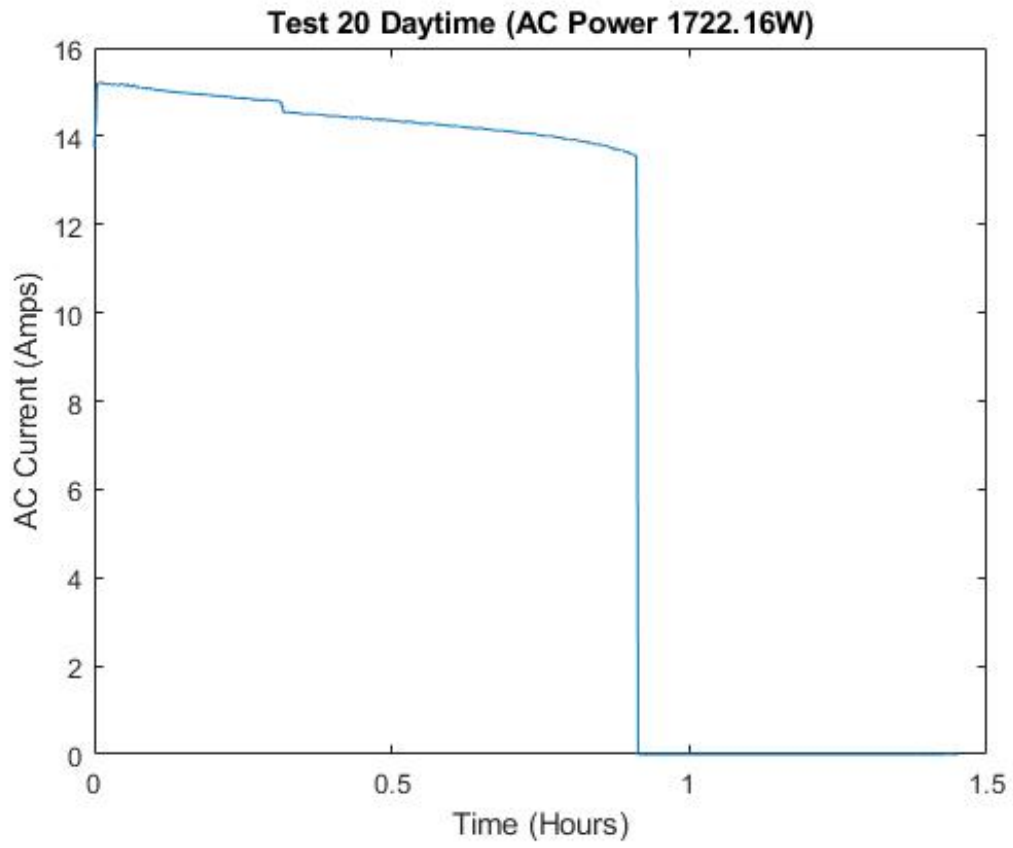


Figure 4.20. Experimental current plot for test 20

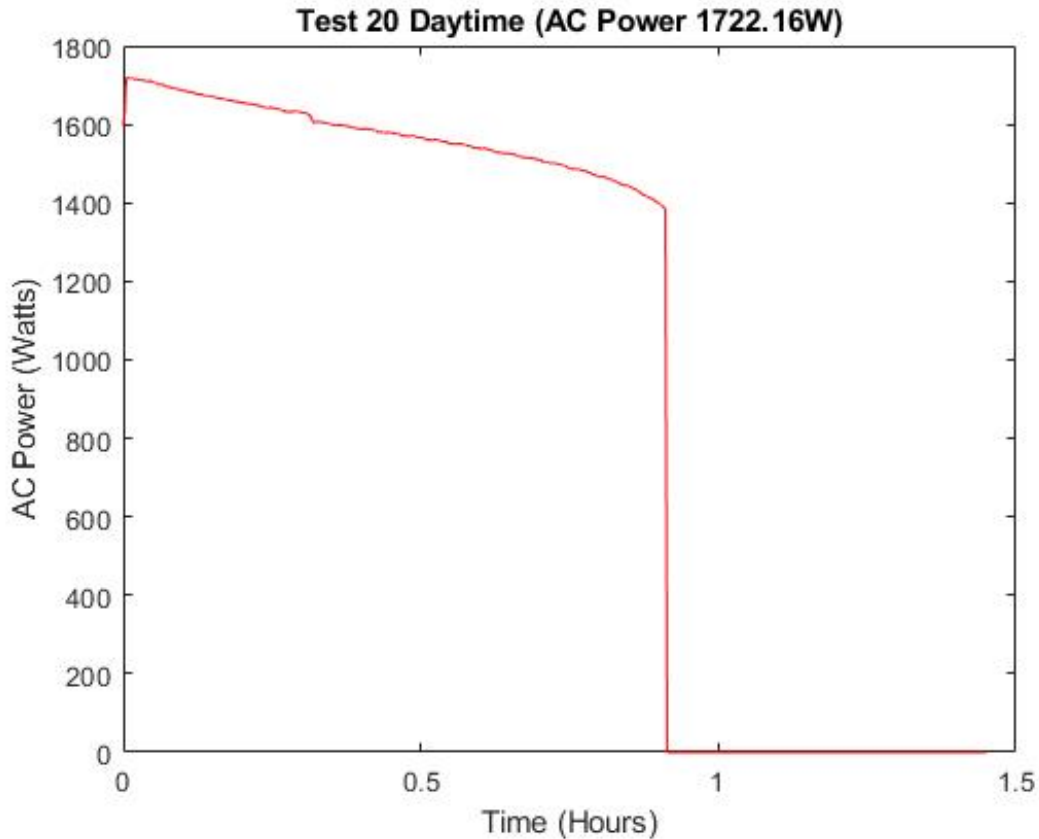


Figure 4.21. Experimental power plot for test 20

The total operating time of the system given 8 different experiments was 56 hours and resulted in no random component failures, the system became unavailable when the batteries were depleted. The number of failures/stoppages of the system was 5.

4.2.3 Resilience Experiments with Configuration 3

The third microgrid configuration includes 8 total PV arrays producing the greatest amount of solar energy of any configuration. The experiments conducted with this configuration are summarized in Table 4.10 (tests 25-34) and follow the same procedure applied to the previous configurations. Figures 4.22 - 4.24 display the results obtained with the experiment conducted at the 608 W power consumption (test 26). It was noticed that the voltage rapidly

oscillated towards the end of the discharge cycle. The DC voltage began to fluctuate at the same rate as the AC voltage until the inverter shut off.

Table 4.10. Experimental data for configuration 3

Test	AC Power Consumption	Time to Failure	Peak Solar Irradiance
25	222 W (AC Critical Load)	15.22 h	1132 W/m ²
26	607.95 W	7.05 h	1075 W/m ²
27	222 W (AC Critical Load)	14.5 h	1066 W/m ²
28	222 W (AC Critical Load)	15.12 h	1080 W/m ²
29	1198.5	2.12 h	1107 W/m ²
30	1198.5 W	1.75 h	1113 W/m ²
31	1198.5 W	2.95 h	1109 W/m ²
32	607.95	7.7 h	1105 W/m ²
33	1722.16 W	1.72 h	1050 W/m ²
34	1722.16 W	0.63 h	1070 W/m ²

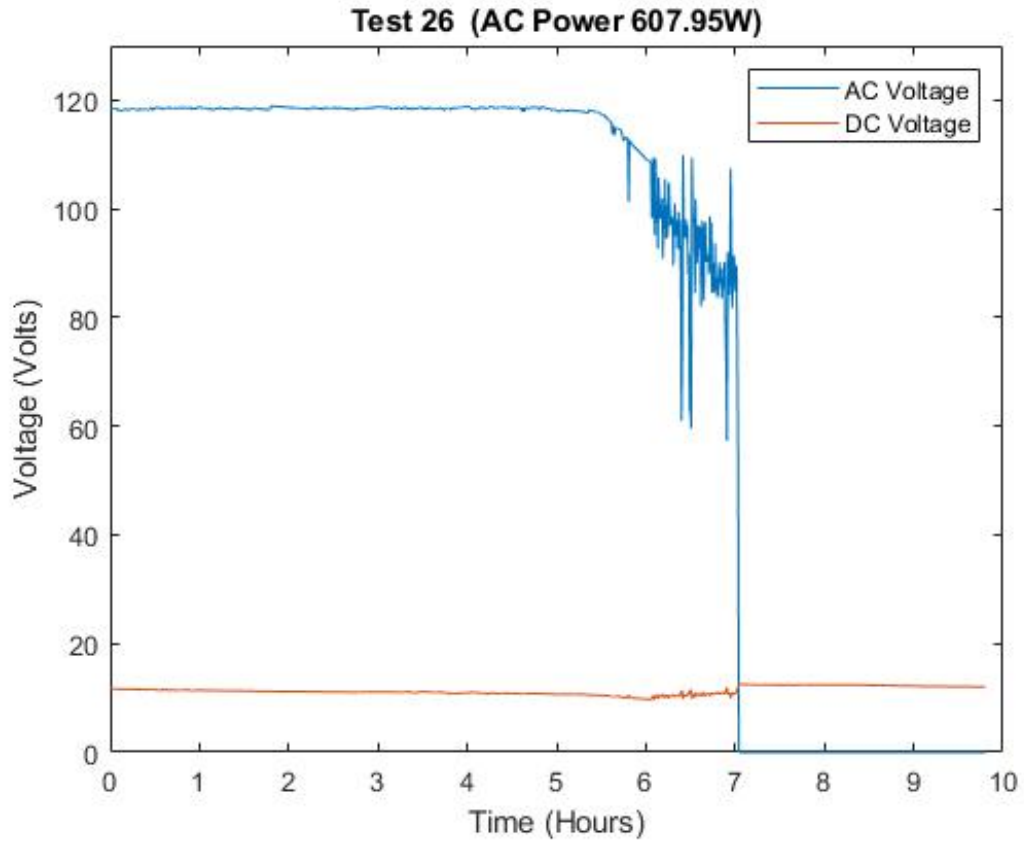


Figure 4.22. Experimental voltage plot for test 26

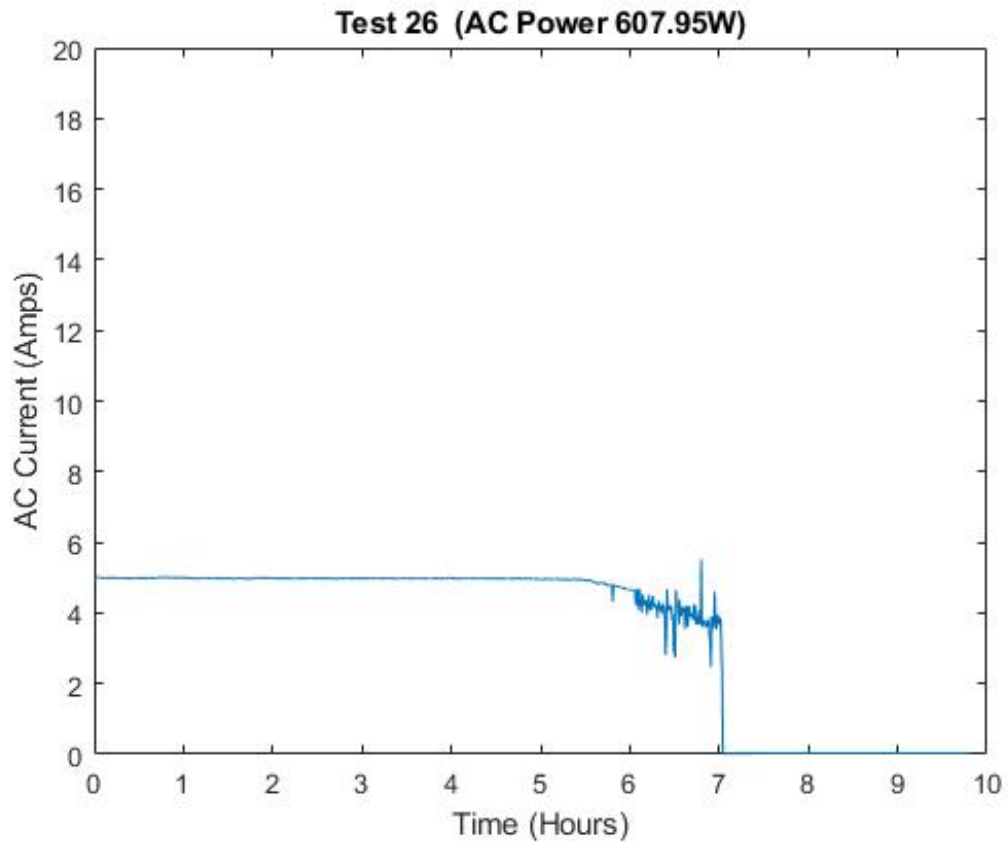


Figure 4.23. Experimental current plot for test 26

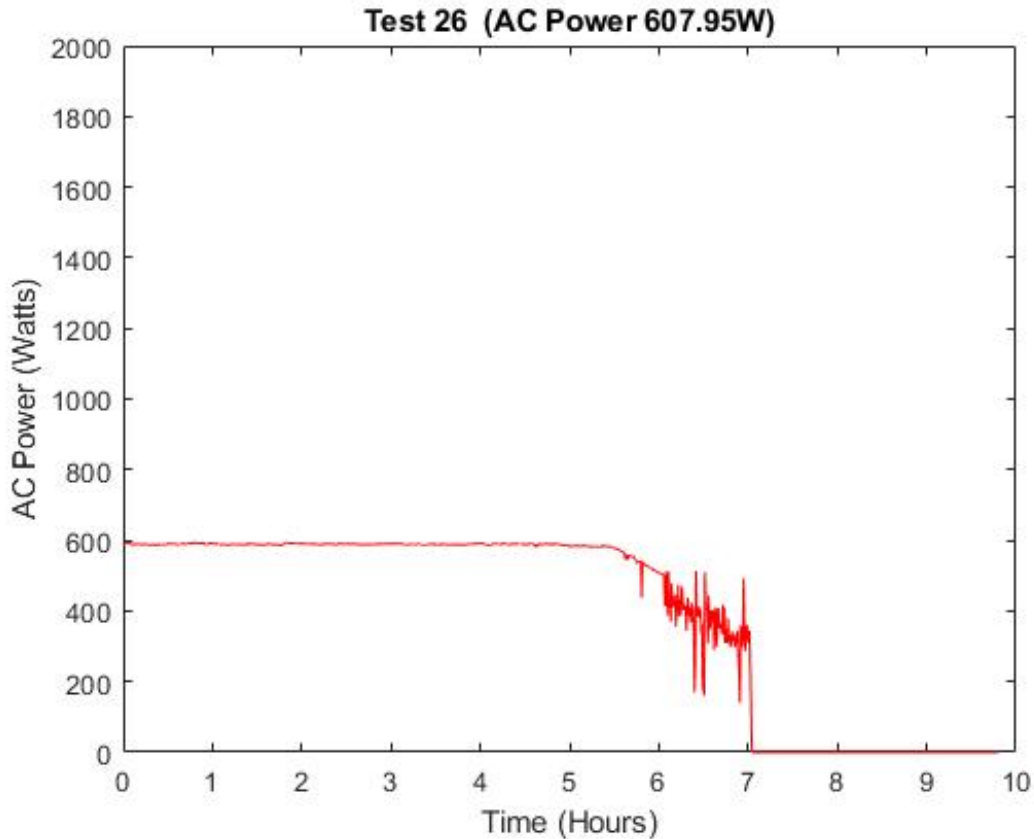


Figure 4.24. Experimental power plot for test 26

The total operating time of the system given 10 different experiments was 69 hours and resulted in no random component failures, just nonavailability of the batteries due to depletion of charge as previously stated. The number of failures/stoppages of the system was 8.

4.3 Microgrid Resilience Analysis

A total of 34 experiments were conducted over the three different configurations resulting in 239 hours of reliability and resilience testing under various load conditions. In the total amount of elapsed time, no components randomly failed. The inverter powered off after reaching the undervoltage limit making the system not available until the batteries could

be recharged for each test. Once the batteries were recharged, the system became available. In analyzing the reliability of each subcomponent of the system based on the load, the critical load reached mission success by providing enough energy to sustain operations throughout day and into the night. However, the critical load would need to be reduced to cover continuous operations. The stand-alone system for each configuration adapted to the changing environment and continued to perform despite multiple simulated faults and continuous testing of the system.

As the critical load is increased, user should keep in mind the sizing of the system in order to ensure enough energy is provided for mission success. Configuration 3 was the most resilient due in part to the 8 PV arrays added to the system providing more input power as displayed in Table 4.11. The added PV arrays charged the ESS at a faster rate than Configurations 1 and 2 which supplied enough energy to the critical load for mission success. Equation (4.3) shows the charging time of the batteries based on the added PV arrays for Configuration 3. This resulted in faster turnaround times for the availability of the system.

$$\text{Battery charging time (h)} = \frac{C_{batt}}{I_{supplied}} = \frac{100 \text{ Ah}}{22 \text{ A}} = \mathbf{4.55 \text{ h.}} \quad (4.3)$$

Table 4.11. Total data for each configuration

Configuration	Total PV Current	Total PV Power	Total BATT Current	Total BATT Power
1	8 A	240 W	10 A	240 W
2	10 A	278 W	22 A	276 W
3	22 A	665 W	49.9 A	659 W

4.4 Availability

Availability is a key aspect in stand-alone microgrid analysis. As previously discussed, operational availability was applicable for this research and was determined based on the maintenance cycle of the subcomponents. The data below depicts the mean maintenance times computed for this experiment. Using equation (2.8) as previously discussed in Section 2.2, the operational availability of the system as described in [16] is

- MTTR = 0.5 hour
- Mean active corrective preventive maintenance time = 0.33 hour
- Mean logistic time = 0.75 hour
- Mean administrative time = 0.4 hour
- MTBM = 79 hours for either corrective or preventive maintenance actions
- RT = 3 hours

$$A_o = \frac{MTBM + RT}{MTBM + RT + MDT} = \frac{79 + 3}{79 + 3 + (0.33 + 0.75 + 0.4)} = \mathbf{0.9823}. \quad (4.4)$$

The COTS products used in this research along with the different configurations allowed the system to meet mission success. A properly sized stand-alone microgrid system that is capable of responding to environmental changes and load fluctuation will supply enough power to support the mission and is a viable option for mobile military units.

CHAPTER 5: CONCLUSION AND FUTURE WORK

This thesis conducted a reliability and resilience analysis of a stand-alone microgrid using COTS DERs products. A multitude of laboratory experiments were designed to experimentally assess the practicality of a stand-alone microgrid to support mobile military units in locations where utility power is not available or is compromised. Three different configurations were designed and tested in the laboratory to observe the performance of the stand-alone microgrid when various faults were simulated to evaluate the time to failure and the overall resilience of the microgrid.

The number of PV arrays were increased for each configuration resulting in greater input power of the system to support the critical load. The critical load, consisting of everyday items found in a household, reached mission success for each configuration because the system was able to supply enough energy to sustain operations. However, the system was not able to sustain operations indefinitely and the microgrid powered off after the inverter reached the undervoltage limit due to the batteries reaching a low state of charge. The third configuration consisting of 8 PV arrays was observed to be the most resilient due in large to the greater amount of solar energy supplied to the system and its ability to recharge the batteries at a faster rate than configurations 1 and 2.

Throughout the experiments, no components randomly failed. The stand-alone microgrid became not available when the batteries fell to a zero state of charge. Upon recharging the batteries to a 100% state of charge, the system became available. This resulted in a theoretical reliability estimate analysis of the system based on a 95% success rate of each subcomponent. Using the exponential model, a reliability estimate of each configuration was determined, it was also shown by having readily available spare parts and maintenance personnel the overall reliability of the system increases. Additionally, operational availability of the system was analyzed based on the various maintenance components to determine the overall availability of the stand-alone microgrid.

5.1 Future Work

The laboratory experiments presented in this thesis should be extended to continue the experimental resilience evaluation of mobile standalone microgrids. Identical and repeated tests should be designed for all configurations to support resilience models and analysis developed in previous work such as [4], [5]. The reliability analysis should be expanded with manufacturer reliability data for the COTS components.

Using the design tools developed by [12], [13] engineers could design other stand-alone microgrid configurations using hybrid ESS to include fuel cells to bridge the gap in coverage at night when no solar energy is available. Hybrid microgrids could also be tested adding a generator to the stand-alone systems analyzed in this thesis.

Additional future work could include testing of DC stand-alone microgrids, where inverters are not required with the consequent increase in overall system reliability as well as efficiency. The DC microgrid testing could be performed using a programmable DC electric load or various DC loads.

List of References

- [1] *Catalyzing Clean Energy Industries and Jobs Through Federal Sustainability*, Executive Order 14057, The President of the USA, Washington, DC, USA, 2021 [Online]. Available: <https://www.govinfo.gov/content/pkg/FR-2021-12-13/pdf/2021-27114.pdf>
- [2] P. Siritoglou and G. Oriti and D.L. Van Bossuyt, “Distributed Energy-Resource Design Method to Improve Energy Security in Critical Facilities,” *Energies*, vol. 14, no. 10, Jul 2021 [Online]. Available: <https://doi.org/10.3390/en14102773>.
- [3] D. Reich and G. Oriti, “Rightsizing the Design of a Hybrid Microgrid,” *Energies*, vol. 14, no. 14, Jul 2021 [Online]. Available: <https://doi.org/10.3390/en14144273>.
- [4] C.J. Peterson and D.L. Van Bossuyt and R.E. Giachetti and G. Oriti, “Analyzing Mission Impact of Military Installations Microgrid for Resilience,” *Systems*, vol. 9, no. 3, Sep 2021 [Online]. Available: <https://doi.org/10.3390/systems9030069>.
- [5] Giachetti, Ronald E. and Bossuyt, Douglas L. Van and Anderson, William and Oriti, Giovanna, “Resilience and Cost Trade Space for Microgrids on Islands,” *IEEE Systems Journal*, pp. 1–11, 2021.
- [6] H. Jiayi, J. Chuanwen, and X. Rong, “A review on distributed energy resources and MicroGrid,” *Renewable and Sustainable Energy Reviews*, vol. 12, no. 9, Dec 2008 [Online]. Available: <https://doi.org/10.1016/j.rser.2007.06.004>.
- [7] A. Muhtadi, D. Pandit, N. Nguyen, and J. Mitra, “Distributed energy resources based microgrid: Review of architecture, control and reliability,” *IEEE Transactions on Industry Applications*, vol. 57, no. 3, May-Jun 2021 [Online]. Available: <https://doi.org/10.1109/TIA.2021.3065329>.
- [8] C.A. Cortes and S.F. Contreras and M. Shahidehpour, “Microgrid Topology Planning for Enhancing the Reliability of Active Distribution Networks,” *IEEE Transactions on Smart Grid*, vol. 9, no. 6, Nov 2018 [Online]. Available: <https://doi.org/10.1109/TSG.2017.2709699>.
- [9] R.H. Lasseter, “Smart Distribution: Coupled Microgrids,” *Proceedings of the IEEE*, vol. 99, no. 6, Jun 2011 [Online]. Available: <https://doi.org/10.1109/JPROC.2011.2114630>.
- [10] Sakshi Mishra and Kate Anderson and Brian Miller and Kyle Boyer and Adam Warren, “Microgrid resilience: A holistic approach for assessing

threats, identifying vulnerabilities and designing corresponding mitigation strategies,” *Applied Energy*, vol. 264, April 2020 [Online]. Available: <https://doi.org/10.1016/j.apenergy.2020.114726>.

- [11] N. Anglani and G. Oriti and R. Fish and D.L. Van Bossuyt, “Design and Optimization Strategy to Size Resilient Stand-Alone Microgrids in Various Climatic Conditions,” in Proc. of IEEE 13th Energy Conversion Congress and Expo (ECCE), Virtual, 2021.
- [12] P. Siritoglou, “Distributed Energy Storage Design and Modeling to Improve the Energy Security of Naval Facilities,” M.S. thesis, Dept. of Natl. Sec. Aff., NPS, Monterey, CA, USA, 2019 [Online]. Available: <http://hdl.handle.net/10945/62817>
- [13] R. Fish, “Design and Modeling of Hybrid Microgrids in Arctic Environments,” M.S. thesis, Dept. of Natl. Sec. Aff., NPS, Monterey, CA, USA, 2020 [Online]. Available: <http://hdl.handle.net/10945/66072>
- [14] X. Song and Y. Zhao and J. Zhou and Z. Weng, “Reliability Varying Characteristics of PV-ESS-Based Standalone Microgrid,” *IEEE Access*, vol. 7, Aug 2019 [Online]. Available: <https://doi.org/10.1109/ACCESS.2019.2937623>.
- [15] *Military Handbook Reliability Prediction of Electronic Equipment*, MIL-HDBK-217F, U.S. Department of Defense, Washington, DC, USA, 1991.
- [16] *Military Handbook Electronic Reliability Design Handbook*, MIL-HDBK-338B, U.S. Department of Defense, Washington, DC, USA, 1998.
- [17] EPA, “Sources of Greenhouse Gas Emissions,” Accessed Aug. 08, 2022 [Online]. Available: <https://www.epa.gov/ghgemissions/sources-greenhouse-gas-emissions>
- [18] F. Dawood and G.M. Shafiullah and M. Anda, “Stand-Alone Microgrid with 100% Renewable Energy: A Case Study with Hybrid Solar PV-Battery-Hydrogen,” *Sustainability*, vol. 12, no. 5, Mar 2020 [Online]. Available: <https://doi.org/10.3390/su12052047>.
- [19] W. Feng, M. Jin, X. Liu, Y. Bao, C. Marnay, C. Yao, and J. Yu, “A review of microgrid development in the United States – A decade of progress on policies, demonstrations, controls, and software tools,” *Applied Energy*, vol. 228, pp. 1656–1668, 2018.
- [20] Y. Song and B. Wang, “Survey on Reliability of Power Electronic Systems,” *IEEE Transactions on Power Electronics*, vol. 28, no. 1, Jan 2013 [Online]. Available: <https://doi.org/10.1109/TPEL.2012.2192503>.

- [21] A. L. Julian and G. Oriti, "A Comparison of Redundant Inverter Topologies to Improve Voltage Source Inverter Reliability," *IEEE Transactions on Industry Applications*, vol. 43, no. 5, pp. 1371–1378, 2007.
- [22] A. L. Julian, G. Oriti, and S. T. Blevins, "Operating Standby Redundant Controller to Improve Voltage-Source Inverter Reliability," *IEEE Transactions on Industry Applications*, vol. 46, no. 5, pp. 2008–2014, 2010.
- [23] J. Jones and J. Hayes, "Estimation of system reliability using a "non-constant failure rate" model," *IEEE Transactions on Reliability*, vol. 50, no. 3, Sep 2001 [Online]. Available: <https://doi.org/10.1109/24.97412>.
- [24] A. Hoyland, *System reliability theory: models and statistical methods*. New York: J. Wiley, 1994.
- [25] A.T. Bryant and P.A. Mawby and P.R. Palmer and E. Santi and J.L. Hudgins, "Exploration of Power Device Reliability Using Compact Device Models and Fast Electrothermal Simulation," *IEEE Transactions on Industry Applications*, vol. 44, no. 3, May-Jun 2008 [Online]. Available: <https://doi.org/10.1109/TIA.2008.921388>.
- [26] M. Ciappa, F. Carbognani, P. Cova, and W. Fichtner, "Lifetime prediction and design of reliability tests for high-power devices in automotive applications," in *2003 IEEE International Reliability Physics Symposium Proceedings, 2003. 41st Annual.*, 2003, pp. 523–528 [Online]. Available: "<https://doi.org/10.1109/RELPHY.2003.1197803>".
- [27] Cushing, M.J. and Mortin, D.E. and Stadterman, T.J. and Malhotra, A., "Comparison of electronics-reliability assessment approaches," *IEEE Transactions on Reliability*, vol. 42, no. 4, Dec 1993 [Online]. Available: <https://doi.org/10.1109/24.273574>.
- [28] D. Murdock, J. Ramos, J. Connors, and R. Lorenz, "Active thermal control of power electronics modules," in *38th IAS Annual Meeting on Conference Record of the Industry Applications Conference, 2003.*, 2003, vol. 3, pp. 1511–1515 vol.3 [Online]. Available: <https://doi.org/10.1109/IAS.2003.1257756>.
- [29] Peugeot, R. and Courtine, S. and Rognon, J.-P., "Fault detection and isolation on a PWM inverter by knowledge-based model," *IEEE Transactions on Industry Applications*, vol. 34, no. 6, Nov-Dec 1998 [Online]. Available: <https://doi.org/10.1109/28.739017>.
- [30] B.S. Blanchard and W.J. Fabrycky, *Systems engineering and analysis*, 5th ed. ed. Upper Saddle River, NJ, USA: Prentice Hall, 2011.

- [31] Tamer Khatib and Ibrahim A. Ibrahim and Azah Mohamed, “A review on sizing methodologies of photovoltaic array and storage battery in a standalone photovoltaic system,” *Energy Conversion and Management*, vol. 120, May 2016 [Online]. Available: <https://doi.org/10.1016/j.enconman.2016.05.011>.
- [32] Monaaf D.A. Al-falahi and S.D.G. Jayasinghe and H. Enshaei, “A review on recent size optimization methodologies for standalone solar and wind hybrid renewable energy system,” *Energy Conversion and Management*, vol. 143, Jul 2017 [Online]. Available: <https://doi.org/10.1016/j.enconman.2017.04.019>.
- [33] Ebaid, Munzer S. Y. and Qandil, Hasan and Hammad, Mahmoud, “Unified approach for designing a photo voltaic solar system for underground water pumping well-34 at Dici aquifer,” *Energy Conversion and Management*, vol. 75, Nov 2013 [Online]. Available: <https://doi.org/10.1016/j.enconman.2013.07.083>.
- [34] mr positive, “Lead Acid Battery Types,” Accessed Aug. 08, 2022 [Online]. Available: <https://www.mrpositive.co.nz/buying/knowledge-base/lead-acid-battery-types/>
- [35] Deng, Da, “Li-ion batteries: basics, progress and challenges,” *Energy Science & Engineering*, vol. 3, no. 5, Aug 2015 [Online]. Available: <https://doi.org/10.1002/ese3.95>.
- [36] Masters, Gilbert M, *Renewable and efficient electric power systems*, 2nd ed ed. New York: Wiley, 2013.
- [37] *Stand-alone Photovoltaic Systems - A Handbook of Recommended Design Practices*, Sandia National Laboratories, U.S. Department of Energy, Albuquerque, New Mexico, USA, 1985. [Online]. Available: http://educyclopedia.karadimov.info/library/sand87_7023.pdf
- [38] Trojan Battery Company, “SPRE 12 225 DS, deep cycle solar flooded battery,” Accessed Aug. 11, 2022 [Online]. Available: https://www.trojanbattery.com/pdf/datasheets/SPRE_12_225_DS.pdf
- [39] Trojan Battery Company, “Motive 8D-AGM Dual Purpose AGM battery,” Accessed Aug. 11, 2022 [Online]. Available: http://www.trojanbattery.com/pdf/datasheets/8DAGM_Trojan_Data_Sheets.pdf
- [40] SimpliPhi Power, “SimpliPhi Phi 3.5, Li-Ion battery, REV061818,” Accessed Aug. 11, 2022 [Online]. Available: <https://simpliphipower.com/documentation/phi-3-5/simpliphi-power-phi-3-5-kwh-60-amp-specification-sheet.pdf>
- [41] Relion Power, “RB 48V 100, Li-Ion battery,” Accessed Aug. 11, 2022 [Online]. Available: https://ceb8596f236225acd007-8e95328c173a04ed694af83ee4e24c15.ssl.cf5.rackcdn.com/docs/product/RELiON-Data-Sheet_RB48V100.pdf

- [42] Relion Power, “RB 48V 100, Li-Ion battery,” Accessed Aug. 11, 2022 [Online]. Available: <https://reliionbattery.com/products/lithium/rb48v150>
- [43] Relion Power, “RB 48V 200, Li-Ion battery,” Accessed Aug. 11, 2022 [Online]. Available: https://ceb8596f236225acd007-8e95328c173a04ed694af83ee4e24c15.ssl.cf5.rackcdn.com/docs/product/RELiON-Data-Sheet_RB48V100.pdf
- [44] EV Power A.S., “Winston LFP400AHA,” Accessed Aug. 11, 2022 [Online]. Available: https://files.gwl.eu/inc/_doc/attach/StoItem/1706/ThunderSky-Winston-LIFEPO4-400Ah-Datasheet.pdf
- [45] EV Power A.S., “Winston LFP7400AHA,” Accessed Aug. 11, 2022 [Online]. Available: https://files.gwl.eu/inc/_doc/attach/StoItem/2157/GWL-Winston-LFP700AHA.pdf
- [46] EV Power A.S., “Winston LFP10400AHC,” Accessed Aug. 11, 2022 [Online]. Available: https://files.gwl.eu/inc/_doc/attach/StoItem/1886/GWL-Winston-LFP1000AHC.pdf
- [47] D. Linden and T.B. Reddy, *Handbook of Batteries*, 3rd ed. ed. New York: McGraw-Hill, 2002.
- [48] Solartech Power, Inc., 90W polycrystalline solar panel, [Online], Accessed July 20, 2022 [Online]. Available: <https://www.solartechpower.com/images/Jseries/SPM090P-BP.pdf>
- [49] EPEVER, MPPT Solar Charge Controller Tracer4210AN model, [Online], Accessed July 20, 2022 [Online]. Available: <https://www.epever.com/upload/cert/file/1811/Tracer-AN-SMS-EL-V1.0.pdf>
- [50] BatteriesPlus, WKDC12-100PUS Werker 12V 100AH Deep Cycle AGM SLA Battery with P Terminals, [Online], Accessed July 20, 2022 [Online]. Available: <https://www.batteriesplus.com/battery/sla-sealed-lead-acid/12/wkdc12=100pus>
- [51] Sensata-Airpax, Circuit Breaker Magnetic-Hydraulic Lever 30A, [Online], Accessed July 20, 2022 [Online]. Available: <https://www.digikey.com/en/products/detail/sensata-airpax/IUGN6-1-51-30-0/14763546>
- [52] AIMS Power, 1500W pure sine wave inverter 24Vdc, [Online], Accessed July 20, 2022 [Online]. Available: <https://www.aimscorp.net/documents/PWRI150012120S%20041921.pdf>
- [53] AIMS Power, 3000W pure sine wave inverter 12Vdc, [Online], Accessed July 20, 2022 [Online]. Available: <https://www.aimscorp.net/documents/PWRI300012120S%20022222.pdf>

- [54] Fluke, Fluke 433/434/435 Three-Phase Power Quality Analyzers, [Online], Accessed July 20, 2022 [Online]. Available: https://dam-assets.fluke.com/s3fs-public/F430-II_umeng0100.pdf
- [55] Fluke, “PowerLog Classic Application Software V4.6 (.exe),” 2018, Accessed Feb 2022 [Online]. Available: <https://www.fluke.com/en-us/support/software-downloads/fluke-powerlog-application-software>
- [56] Solar Energy Local, “Solar Energy in Monterey, CA,” Accessed Jul. 29, 2022 [Online]. Available: <https://www.solarenergylocal.com/states/california/monterey/>
- [57] altE, “Solar Maps for the USA,” Accessed Aug. 04, 2022 [Online]. Available: <https://www.altestore.com/diy-solar-resources/solar-insolation-map-usa/>
- [58] Emporis, Accessed August 17, 2022 [Online]. Available: <https://www.emporis.com/buildings/223223/spanagel-hall-monterey-ca-usa>

Initial Distribution List

1. Defense Technical Information Center
Ft. Belvoir, Virginia
2. Dudley Knox Library
Naval Postgraduate School
Monterey, California